

Skyrme-Hartree-Fock-Bogoliubov mass models on a 3D mesh: III. From atomic nuclei to neutron stars

Guilherme Grams^{a,1}, Wouter Ryssens¹, Guillaume Scamps², Stephane Goriely¹, Nicolas Chamel¹

¹Institut d'Astronomie et d'Astrophysique, Université Libre de Bruxelles, Brussels, Belgium

²Department of Physics, University of Washington, Seattle, USA.

Received: date / Accepted: date

Abstract We present BSkG3, the latest entry in the Brussels-Skyrme-on-a-grid series of large-scale models of nuclear structure based on an energy density functional. Compared to its predecessors, the new model offers a more realistic description of nucleonic matter at the extreme densities relevant to neutron stars. This achievement is made possible by incorporating a constraint on the infinite nuclear matter properties at high densities in the parameter adjustment, ensuring in this way that the predictions of BSkG3 for the nuclear Equation of State are compatible with the observational evidence for heavy pulsars with $M > 2M_{\odot}$. Instead of the usual phenomenological pairing terms, we also employ a more microscopically founded treatment of nucleon pairing, resulting in extrapolations to high densities that are in line with the predictions of advanced many-body methods and are hence more suited to the study of superfluidity in neutron stars. By adopting an extended form of the Skyrme functional, we are able to reconcile the description of matter at high densities and at saturation density: the new model further refines the description of atomic nuclei offered by its predecessors. A qualitative improvement is our inclusion of ground state reflection asymmetry, in addition to the spontaneous breaking of rotational, axial, and time-reversal symmetry. Quantitatively, the model offers lowered root-mean-square deviations on 2457 masses (0.631 MeV), 810 charge radii (0.0237 fm) and an unmatched accuracy with respect to 45 primary fission barriers of actinide nuclei (0.33 MeV). Reconciling the complexity of neutron stars with those of atomic nuclei establishes BSkG3 as a tool of choice for applications to nuclear structure, the nuclear equation of state and nuclear astrophysics in general.

Keywords energy density functional · neutron star · equation of state

1 Introduction

Nucleons in limited numbers can form self-bound composite objects: atomic nuclei composed of up to 238 nucleons occur naturally on earth while heavier isotopes, up to ^{294}Og so far, can be synthesised in accelerators [1]. The properties of nuclei are directly relevant to astrophysics: nuclear reactions and decays produce the energy that powers stars throughout their evolution [2]. Although reaction rates are strongly influenced by temperature and extremely neutron-rich systems can be produced in violent phenomena, in most astrophysical conditions atomic nuclei remain the relevant organisational unit of nucleons with central densities never deviating much from saturation $\rho_{\text{sat}} \approx 0.16 \text{ fm}^{-3}$.

Neutron stars (NSs), exotic and extremely compact objects created in the gravitational core-collapse of massive stars at the end of their lives are notable exceptions: these stars contain about 10^{57} nucleons under extreme gravitational pressure. Their interior is stratified into distinct layers, each of which features a different arrangement of protons and neutrons. The surface of cold-catalyzed NSs is believed to be covered by an ocean of ^{56}Fe and neighboring elements ¹ while the layers beneath are solid and composed of highly exotic nuclei that become progressively more neutron-rich with increasing depth [4]. The point at which neutrons start to drip out of nuclei delimits the boundary

¹The case of accreting NSs is more complex: their surface also contains light elements such as hydrogen and helium transferred from the stellar companion, and heavier elements produced by thermonuclear explosions, see e.g. Ref. [3] and references therein.

^ae-mail: guilherme.grams@ulb.be

between the outer and inner crust where a liquid of free neutrons coexists with neutron-rich clusters containing hundreds of nucleons [4]. The dissolution of the crust at about half saturation density marks the transition to the core, which consists of a liquid mixture of protons, neutrons, and leptons. The composition of the inner part of the core in the most massive NSs remains uncertain. Near the crust-core transition, some models predict the existence of a nuclear pasta mantle where neutrons and protons form exotic structures such as long cylinders (‘spaghetti’) or plates (‘lasagna’) due to Coulomb frustration [5, 6]. The Equation of State (EoS) of dense matter, *i.e.*, the thermodynamical relation between the mean energy density of matter and pressure, is the key microscopic ingredient to determine the macroscopic properties of a NS [7].

Understanding the properties of matter in all astrophysical environments is an enormous challenge. Even near saturation density, the difficulty of creating and handling radioactive isotopes implies that experimental efforts cannot possibly measure the properties of all relevant isotopes and reactions. So far, the only earth-based method capable of investigations beyond saturation density relies on relativistic collisions of heavy ions to produce high-density nucleonic matter that is out of equilibrium for most of its extremely short lifespan [8, 9].

Given these experimental difficulties, it falls to nuclear theory to build models that are capable of extrapolation to all relevant regimes. Ideally, a single model would provide us with a complete EoS, *i.e.* one that spans the enormous range from below saturation density to that prevailing in the core of NSs for arbitrary proton-neutron asymmetry, but also with all properties of nuclear structure that are relevant to the modelling of nuclear reactions and decays, from binding energies to more complicated quantities such as nuclear level densities, optical potentials, or strength functions [10]. A complete description is particularly desirable to explore nucleosynthesis through the so-called rapid neutron capture process or r-process: when NSs collide, neutron-capture reactions and decays of different kinds compete to transform any ejected matter into heavy elements. The combined observation of both the gravitational waves emitted by such an event and the electromagnetic radiation emitted by the ejected matter, the kilonova [11], has recently confirmed NS mergers as a locus of r-process nucleosynthesis [12].

The complexity of the nucleon-nucleon interaction and the quantum many-body problem renders a complete description of nucleonic matter a daunting task, so much that all models rely on at least a few phenomenological ingredients. The dependence on the latter should however be minimized to gain a measure of confidence

in our extrapolations to unknown regimes: it is essential to derive the emergent properties of nucleonic matter from the microscopic physics of the nucleon-nucleon interaction as much as possible. Ab initio approaches arguably come closest to this ideal but are limited (i) in nucleon number in the case of nuclei [13] despite recent progress [14] and (ii) to densities not much higher than saturation in the case of infinite homogeneous nuclear matter (INM) [15].

Self-consistent models based on nuclear energy density functionals (EDFs) provide an alternative: they offer a quantum description of any nuclear system in terms of its constituent neutrons and protons that is sufficiently tractable for application to the entirety of the nuclear chart and the different regions of NSs [16]. The key to the success of such models is their (comparatively) simple formulation in terms of the nucleonic densities connected to an effective nucleon-nucleon interaction, enabling both the accurate modeling of nuclear properties at the basic mean-field level and applications to INM. Purely theoretical considerations are typically not sufficient to guide the construction of such an analytical form: in practice one adopts a phenomenological form with free parameters that are adjusted to nuclear data². To ensure that predictions are as reliable as possible, those data should be carefully selected and as comprehensive as possible. This includes measurements of a variety of properties of a wide range of nuclei, from stable to exotic neutron-rich isotopes, but also information on the EoS up to a few times saturation density as obtained from heavy-ion collisions or ab initio calculations. Astrophysical observations of NSs of masses above $2M_{\odot}$ provide an additional constraint at even higher densities.

We have recently started the development of a new set of models based on EDFs of the Skyrme type: the Brussels-Skyrme-on-a-Grid (BSkG) series [21]. Like their predecessors, the BSk-family [22, 23], the BSkG models aim to provide a global description of nuclear structure that is as microscopic as possible, with the specific focus of providing input for astrophysical applications. Since differences of binding energies set the energy scale for all nuclear reactions and decays, the objective function for these models included all known nuclear masses of nuclei with $N, Z \geq 8$. As a result, the BSkG1 [21] and BSkG2 [24] models achieved a root-mean-square (rms) deviation with respect to 2457 known masses of

²The density matrix expansion of Negele and Vautherin [17] and other similar techniques [18] provide a way to derive an analytical form starting from a parameterisation of the bare nucleon-nucleon interaction. This has not found widespread adoption for a variety of reasons but has for instance been used in Refs. [19, 20] to derive an EDF from on chiral effective field theory, although not without free parameters.

0.741 and 0.678 MeV, respectively, which is competitive with more phenomenological models [25]. Most other EDF-based models are adjusted to a limited number of (often spherical) nuclei and typically do not reach this level of accuracy despite the wide variety of EDF forms and fitting protocols available in the literature; Refs. [20, 26–40] form a (necessarily non-exhaustive) set of recent examples. On the other hand, dedicated mass models augmented with machine learning techniques can reach rms deviations lower than 0.1 MeV [41] but such approaches lack the reach in terms of additional observables that EDF-based models can offer. The BSkG-series combines the reproduction of known masses with, among other things, an excellent global description of known charge radii, the systematics of nuclear deformation and the fission properties of actinide nuclei [42].

Crucial to the success of all self-consistent EDF-based models is the concept of spontaneous symmetry breaking: by allowing for deformed mean-field configurations that do not respect all symmetries of nature, such models can grasp a large part of the effect of nuclear collectivity³ while remaining at the mean-field level and thus keeping global calculations tractable. Large-scale EDF-based models have accounted for rotational symmetry breaking and the appearance of nuclear deformation for a few decades now [43], but have not moved beyond the assumption of axial symmetry before the advent of BSkG1, which was the first large-scale EDF-based model to consistently employ a three-dimensional representation of the nucleus, thereby exploring the physics of triaxial deformation on the scale of the nuclear chart [21]. With BSkG2 we went even further, allowing odd-mass and odd-odd nuclei to spontaneously break time-reversal symmetry and benchmarking the influence of spin and current densities and the so-called ‘time-odd’ terms in the Skyrme EDF they contribute to on a global scale [24].

Despite the quality of their description of nuclei, BSkG1 and BSkG2 are not quite satisfactory for the study of NSs for two reasons. First is the incompatibility of their predictions with observations of NSs: BSkG1 and BSkG2 each produce EoSs that lead to a maximum NS mass of about $1.8M_{\odot}$ and thus are incompatible with the existence of heavy pulsars whose mass exceeds $2M_{\odot}$, such as J1614-2230 and J0740+662 [44–46]. A second deficiency is their treatment of pairing: like most Skyrme models, BSkG1 and BSkG2 rely on a sim-

ple and entirely phenomenological ansatz for the pairing terms of the EDF. If the relevant parameters are constrained on the properties of finite nuclei, such an approach leads to unrealistically large 1S_0 pairing gaps in pure neutron matter when compared to advanced many-body treatments of the latter. A realistic description of pairing is particularly relevant to the inner crust and outer core of NSs, with implications for various astrophysical phenomena [47–49].

We present here BSkG3, a new entry in the BSkG-series that addresses these limitations, and is thus much better suited to the study of NSs than its predecessors. To achieve this, we rely on ideas that were already employed by some of the latest BSk-models: i) we use a more microscopically-grounded treatment of nucleon pairing that reproduces the 1S_0 pairing gaps in INM as predicted by extended Brueckner-Hartree-Fock calculations [50, 51], and ii) we force the model to accommodate the existence of heavy pulsars by constraining the EoS at high densities [52]. Such constraints are difficult to reconcile with a competitive global reproduction of masses when relying on a Skyrme EDF of the traditional form: for this reason, we move here to the extended form proposed in Refs. [23, 52].

We also further leverage the power of symmetry breaking: we now allow nuclei to take reflection asymmetric shapes with finite octupole deformation. Combined with the breaking of rotational, axial and time-reversal symmetries, this makes our calculations the most general global study of octupole deformation to date and the first to systematically include odd-mass and odd-odd nuclei. We find that static octupole deformation is only relevant to ground states in specific regions of the nuclear chart, confirming the expectations of earlier studies [53–55]. The impact of this degree of freedom as measured by the global accuracy of our model for masses and radii is thus limited, but it does strongly affect the binding energy of exotic neutron-rich nuclei near $N \sim 196$, possibly affecting the simulations of r-process nucleosynthesis. It also allows our model to connect to the experimental body of evidence of reflection asymmetry in nuclear ground states such as the occurrence of rotational bands of alternating parity [56].

This paper is organized as follows: we first discuss the model ingredients of BSkG3 in Sec. 2, focusing on the differences with preceding models of the BSk- and BSkG-series. Sec. 3 details the adjustment of the model parameters. We report the final values of the latter in Sec. 4 and discuss in detail the models performance with respect to several properties of atomic nuclei. We study the INM predictions of the new model in Sec. 5 and link these to the structure of NS in Sec. 6, reserving our conclusions and outlook for Sec. 7. We provide a list

³Though we note that spontaneous symmetry breaking cannot fully account for all types of collective motion, even if completely symmetry-unrestricted global calculations would be feasible. Global models tacitly assume that the model parameters can absorb most of the missing physics and/or include phenomenological corrections. We do both, see Sec. 2.

of abbreviations and acronyms we use in Appendix A, the complete definition of all EDF coupling constants in terms of model parameters in Appendix B, as well as the equations for the rotational, vibrational and Wigner energies in Appendix C and an explanation of the tables of our results that we provide as supplementary material in Appendix D.

2 Ingredients of the mass model

2.1 The nuclear binding energy and atomic mass

We represent an atomic nucleus with N neutrons and Z protons with a many-body state of the Bogoliubov type, whose total energy E_{tot} we define as:

$$E_{\text{tot}} = E_{\text{HFB}} + E_{\text{corr}}. \quad (1)$$

We call E_{HFB} the mean-field energy and E_{corr} is a set of corrections that account (approximately) for correlations that cannot be captured by single mean-field reference state constructed from separate neutron and proton orbitals. More precisely, the mean-field energy consists of five parts:

$$E_{\text{HFB}} = E_{\text{kin}} + E_{\text{Sk}} + E_{\text{pair}} + E_{\text{Coul}} + E_{\text{cm}}^{(1)}, \quad (2)$$

which are, respectively, the kinetic energy, Skyrme energy, pairing energy, Coulomb energy and the one-body part of the centre-of-mass correction [57]. The correction energy E_{corr} is written in terms of four parts:

$$E_{\text{corr}} = E_{\text{rot}} + E_{\text{vib}} + E_{\text{cm}}^{(2)} + E_{\text{W}}, \quad (3)$$

which are, respectively, the rotational correction, the vibrational correction, the two-body part of the centre-of-mass correction [57], and the Wigner energy [58]. We will also refer to E_{corr} as the collective correction. The total energy E_{tot} is minus the binding energy of the nucleus; the atomic mass $M(N, Z)$ of an atom composed of this nucleus and Z electrons is then given by

$$M(N, Z) = E_{\text{tot}} + NM_n + Z(M_p + M_e) - B_e(Z). \quad (4)$$

In this equation, $M_{n/p}$ are the masses of free neutrons and protons, M_e is the mass of an electron and $B_e(Z)$ is a simple analytical estimate for the binding energy of the electrons [59, 60].

Most model ingredients in Eqs. (2) and (3) are identical to those employed in the BSkG1 and BSkG2 models. There are however two exceptions compared to the preceding models: (i) we employ a more general form of the Skyrme EDF and (ii) we rely on a less phenomenological treatment of the pairing energy. The rest of this section discusses these two differences in detail. For a more detailed description of all other model ingredients, we refer the interested reader to Refs. [21, 24].

2.1.1 The Skyrme energy

As is standard practice, we write the Skyrme energy as an integral over four energy densities $\mathcal{E}_{t,e/o}(\mathbf{r})$:

$$E_{\text{Sk}} = \int d^3\mathbf{r} \sum_{t=0,1} [\mathcal{E}_{t,e}(\mathbf{r}) + \mathcal{E}_{t,o}(\mathbf{r})], \quad (5)$$

where $t = 0, 1$ is an isospin index. Different terms in the energy densities are combinations of different local densities and their derivatives: we employ the set $(\rho_t(\mathbf{r}), \tau_t(\mathbf{r}), \mathbf{J}_t(\mathbf{r}), \mathbf{s}_r(\mathbf{r}), \mathbf{j}_r(\mathbf{r}))$, whose definitions are standard in the literature [61]. The first three densities are even under time-reversal, while the latter two are odd. Since the energy densities themselves are necessarily time-even under time-reversal, their constituent terms can be separated in those bilinear in the time-even densities ($\mathcal{E}_{t,e}(\mathbf{r})$) and those bilinear in the time-odd densities ($\mathcal{E}_{t,o}(\mathbf{r})$).

Seventeen model parameters, *i.e.* six pairs (t_i, x_i) ($i = 0, \dots, 5$) together with three exponents α, β and γ and two spin-orbit parameters W_0 and W'_0 , specify sixteen coupling constants $\{C_t\}$, ten of which depend on the isoscalar density $\rho_0(\mathbf{r})$. Dropping the position-dependence of the latter to lighten notation for coupling constants, we employ the energy densities:

$$\begin{aligned} \mathcal{E}_{t,e}(\mathbf{r}) = & C_t^{\rho\rho}(\rho_0) \rho_t^2(\mathbf{r}) + C_t^{\rho\tau}(\rho_0) \rho_t(\mathbf{r}) \tau_t(\mathbf{r}) \\ & + C_t^{\rho\nabla J} \rho_t(\mathbf{r}) \nabla \cdot \mathbf{J}_t(\mathbf{r}) \\ & + C_t^{\rho\Delta\rho} \rho_t(\mathbf{r}) \Delta\rho_t(\mathbf{r}) \\ & + C_t^{\nabla\rho\nabla\rho}(\rho_0) \nabla\rho_t(\mathbf{r}) \cdot \nabla\rho_t(\mathbf{r}) \\ & + C_t^{\rho\nabla\rho\nabla\rho}(\rho_0) \rho_t(\mathbf{r}) \nabla\rho_0(\mathbf{r}) \cdot \nabla\rho_t(\mathbf{r}) \end{aligned} \quad (6)$$

$$\begin{aligned} \mathcal{E}_{t,o}(\mathbf{r}) = & C_t^{ss}(\rho_0) \mathbf{s}_t(\mathbf{r}) \cdot \mathbf{s}_t(\mathbf{r}) + C_t^{jj}(\rho_0) \mathbf{j}_t(\mathbf{r}) \cdot \mathbf{j}_t(\mathbf{r}) \\ & + C_t^{j\nabla s} \mathbf{j}_t(\mathbf{r}) \cdot \nabla \times \mathbf{s}_t(\mathbf{r}). \end{aligned} \quad (7)$$

Eqs. (6) and (7) differ from the energy densities of BSkG2: the final two terms in Eq. (6) did not appear in Ref. [24] and the coupling constants $C_r^{\rho\tau}(\rho_0)$ and $C_t^{jj}(\rho_0)$ were not density-dependent. This extended form of the Skyrme EDF arises naturally if one generalizes the terms involving t_1 and t_2 in the standard functional to depend on the density: the relevant new parameters are $t_4, x_4, t_5, x_5, \beta$ and γ . This generalization was already incorporated in the latest BSk models [23] but is at the time of writing not widely spread.

In terms of the short-hands $C_{0t}^{+/-}(t, x)$ defined in Appendix B, we write for the time-even part of the EDF

$$C_t^{\rho\tau}(\rho_0) = +\frac{1}{2}C_{0t}^+(t_1, x_1) + \frac{1}{2}C_{0t}^-(t_2, x_2) + \frac{1}{2}C_{0t}^+(t_4, x_4)\rho_0^\beta + \frac{1}{2}C_{0t}^-(t_5, x_5)\rho_0^\gamma, \quad (8)$$

$$C_t^{\nabla\rho\nabla\rho}(\rho_0) = +\frac{3}{8}C_{0t}^+(t_4, x_4)\rho_0^\beta - \frac{1}{8}C_{0t}^-(t_5, x_5)\rho_0^\gamma, \quad (9)$$

$$C_t^{\rho\nabla\rho\nabla\rho}(\rho_0) = -\frac{1}{2}C_{0t}^+(t_4, x_4)\rho_0^{\beta-1}. \quad (10)$$

In the time-odd part, only the term C_t^{jj} is affected by the new parameters: the requirement of local gauge invariance imposes that $C_t^{jj}(\rho_0) = -C_t^{\rho\tau}(\rho_0)$ [62]. The expressions for all other coupling constants in terms of the model parameters (t_i, x_i) ($i = 0, \dots, 3$) are identical to those of BSkG2, we repeat them for completeness in Appendix B. However, we draw the attention of the reader to a change in notation compared to the previous BSkG models: here we associate the exponent γ with the coupling constants in Eqs. (8)-(10) while in Refs. [21, 24] the same symbol determined the density dependence of $C_t^{\rho\rho}(\rho_0)$.

The form of the EDF we employ here is directly inspired by that of Ref. [52] and, as we will show, shares its chief advantage in that it allows for a stiff EoS of neutron matter (NeutM) in combination with an excellent mass fit. However, there are a few differences. First, we do not include any term quadratic in the spin-current density $J_{\mu\nu}(\mathbf{r})$ nor its time-odd counterpart of the form $\mathbf{s}_t(\mathbf{r}) \cdot \mathbf{T}_t(\mathbf{r})$. Second, we do not include any term involving a gradient of the spin density $\mathbf{s}_t(\mathbf{r})$, as these have a tendency to induce unphysical finite-size instabilities [63]. We adhered to these policies for the standard Skyrme functional for the construction of BSkG1 and BSkG2, and apply them here equally to the generalized EDF form of Ref. [52].

Aside from these omitted terms, there are seemingly further differences between our formulation of the energy densities in Eqs. (6–7) and their counterparts in Ref. [52]. These differences are of no consequence however: one can use partial integration under the integral sign of Eq. (5) to recombine the various gradients in the energy densities in different ways, leading to many different expressions for $\mathcal{E}_{t,e/o}(\mathbf{r})$ that are not identical yet physically equivalent. Eqs (6) and (7) are the expressions we found most convenient for numerical implementation.

2.1.2 The pairing energy

We supplement the Skyrme form in the particle-hole channel with the following density-dependent pairing

functional:

$$E_{\text{pair}} = \frac{1}{4} \sum_{q=p,n} \int d^3\mathbf{r} g_q(\rho_n, \rho_p) \tilde{\rho}_q^*(\mathbf{r}) \tilde{\rho}_q(\mathbf{r}), \quad (11)$$

where $\tilde{\rho}_q(\mathbf{r})$ is the pairing density of species $q = p, n$. Although the definition of this density is somewhat standard in the literature, see for example Ref. [61], it is not often mentioned that it does not have a definite behaviour under time-reversal: its real part is time-even while its complex part is time-odd [24]. To avoid the ultra-violet divergence of Eq. (11), we calculate the pairing density in the single-particle basis which diagonalises the single-particle hamiltonian and weight the contribution of each state with single-particle energy ϵ to the pairing density with the following cutoff function:

$$f_q = \left[1 + e^{(\epsilon - \lambda_q - E_{\text{cut}})/\mu} \right]^{-1/4}, \quad (12)$$

where λ_q is the Fermi energy of species q , E_{cut} is an adjustable parameter of the model and we fix $\mu = 0.5$ MeV. Note that Eq. (12) eliminates the contribution from states at high energy but does not significantly affect states below the Fermi energy; note that this differs from our choice of cutoff for the preceding models.

Both BSkG1 and BSkG2 rely on a widely-used empirical form for the function $g_q(\rho_n, \rho_p)$:

$$g_q(\rho_n, \rho_p) = V_{\pi q} \left[1 - \eta \left(\frac{\rho_0(\mathbf{r})}{\rho_{\text{ref}}} \right)^\xi \right], \quad (13)$$

where $\eta, \xi, V_{\pi p}$ and $V_{\pi, n}$ are adjustable parameters⁴ and the reference density is typically fixed at $\rho_{\text{ref}} = 0.16$ fm⁻³. Despite its success for pairing-related quantities in nuclei, this recipe is not suited to NSs applications for two reasons. First, assuming $V_{\pi q}$ is negative, Eq. (13) describes a transition to a regime of repulsive pairing for $\rho_0(\mathbf{r}) \geq \rho_{\text{ref}}/\eta^\alpha$. The parameter values of BSkG1 and BSkG2 imply this unphysical transition happens at 0.258 and 0.396 fm⁻³, i.e. in density regimes that exist in low- and medium-mass NSs.

The second, less obvious, reason is that when the parameters of empirical forms such as Eq. (13) are adjusted to the properties of nuclei, the resulting pairing gaps in INM are qualitatively different from the predictions of more advanced many-body methods. To illustrate this point, we show in Fig. 1 the neutron ¹S₀ pairing gaps Δ_n in NeutM as a function of the density ρ_n for the BSkG1 and BSkG2 models and compare them to the predictions of several references: the extended Brueckner-Hartree-Fock (BHF) calculations

⁴Refs. [21, 24] employ the symbol α instead of ξ for the exponent in Eq. (13). We change notation here to avoid confusion with the exponents in the particle-hole channel of the EDF.

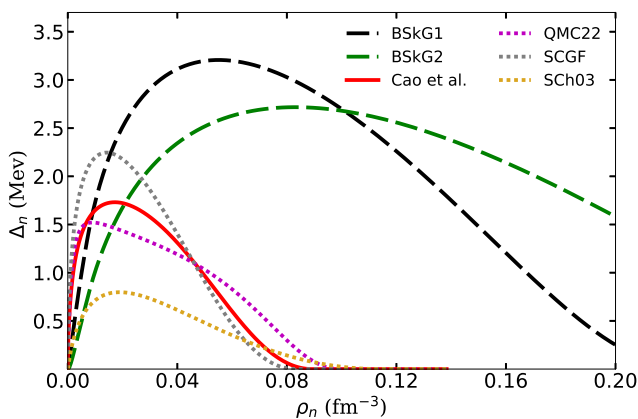


Fig. 1 1S_0 pairing gaps Δ_n in NeutM as a function of the neutron density ρ_n : from Cao et al. [50] (red full line), QMC22 [64] (magenta dotted line), SCGF [65] (gray dotted line), SCh03 [66] (yellow dotted line), MB23 [67] (brown dotted line), BSkG1 (black dashed line) and BSkG2 (green dashed line). The curves for BSk31 and BSkG3 are equal to the results of Cao et al. by construction.

of Ref. [50], the calculations based on renormalization group theory (SCh03) of Ref. [66] and more recent results obtained with Quantum Monte Carlo techniques (QMC22) [64], self-consistent Green’s functions (SCGF) [65] and a diagrammatic method (MB23) [67]. Although there is a certain spread in the predictions of the advanced many-body calculations, it is immediately obvious that the predictions of BSkG1 and BSkG2 largely fall outside this spread. The empirical pairing terms employed by both BSkG1 and BSkG2 (as well as most of the standard volume and/or surface pairing interactions used in the framework of Skyrme-HFB calculations) result in large pairing gaps up to 3 MeV that persist up to high densities while more microscopic approaches produce gaps that are generally smaller than 2 MeV and quickly decay beyond $\rho_n \sim 0.05 \text{ fm}^{-3}$.

To address these deficiencies, we discard the phenomenological ansatz for $g_q(\rho_n, \rho_p)$ and rely instead on the approach of Refs. [51,68]: it allows our new model to reproduce exactly any given set of pairing gaps in INM, $\Delta_q^{\text{INM}}(\rho_n, \rho_p)$. We repeat the choice made for BSk31 [23] and take as starting point the INM pairing gaps of Ref. [50], thereby essentially forcing BSkG3 to reproduce the solid red curve in Fig. 1. Ref. [50] only provides gap for symmetric ($\Delta_{\text{sm}}^{\text{INM}}$) and pure neutron matter ($\Delta_{\text{nm}}^{\text{INM}}$), which forces us to adopt an interpolation recipe to obtain the gap at arbitrary asymmetry δ :

$$\Delta_q^{\text{INM}}(\rho_n, \rho_p) = (1 - |\delta|)\Delta_{\text{sm}}^{\text{INM}}(\rho_0) + |\delta|\Delta_{\text{nm}}(\rho_q). \quad (14)$$

This linear interpolation is entirely empirical due to the lack of guidance from advanced many-body approaches, but guarantees positive gaps for arbitrary δ .

We now start from the following ansatz for the function g_q :

$$g_q(\rho_n, \rho_p) = V_q(\rho_n, \rho_p) [1 + \kappa_q(\nabla\rho_0)^2], \quad (15)$$

where the κ_q are adjustable parameters and $V_q(\rho_n, \rho_p)$ are the “pairing strengths” which reproduce the (interpolated) INM pairing gaps (Eq. 14). These strengths can be calculated via [51, 68]:

$$V_q(\rho_n, \rho_p) = -\frac{8\pi^2}{I_q(\rho_n, \rho_p)} \left(\frac{\hbar^2}{2M_q^*(\rho_n, \rho_p)} \right)^{3/2}, \quad (16)$$

where

$$I_q = \int_0^{\lambda_q^{\text{INM}} + E_{\text{cut}}} d\xi \frac{\sqrt{\xi}}{\sqrt{(\xi - \mu_q)^2 + [\Delta_q^{\text{INM}}(\rho_n, \rho_p)]^2}}. \quad (17)$$

In Eq. (16), $M_q^*(\rho_n, \rho_p)$ is the position-dependent effective mass of species q defined through

$$\frac{\hbar^2}{2M_q^*(\rho_n, \rho_p)} = \frac{\hbar^2}{2m_q} + \sum_{t=0,1} \frac{\partial \mathcal{E}_{t,e}}{\partial \tau_q}. \quad (18)$$

We calculate the functional derivative in Eq. (18) consistently from the Skyrme EDF, that is to say from the equations presented in Sec. 2.1.1⁵. The integral in Eq. (17) depends on the Fermi energy in INM λ_q^{INM} , which we estimate using the Fermi wave-number [68]:

$$\lambda_q^{\text{INM}} \approx \frac{\hbar^2 k_{F,q}}{2M_q^*} = \frac{\hbar^2}{2M_q^*} (3\pi^2 \rho_q)^{1/3}. \quad (19)$$

For our three-dimensional representation, the numerical integration of Eq. (17) for each mesh point would become costly. To avoid this, we employ the analytical approximation for I_q of Ref. [68] that was also used for some of the later entries in the BSk family [23].

The parameters κ_q play no role in all of these considerations since all gradients of the density vanish identically in INM. They are nevertheless crucial to the overall success of our model: without the κ_q we would likely not have been able to reproduce the pairing properties of finite nuclei [23] from the realistic pairing gaps in INM (as already inferred from Fig. 1). The reason is that all advanced many-body calculations produce pairing gaps that are small for neutron densities that are encountered near the surface of finite nuclei and essentially vanishes for densities typically found near their centre, $\rho \sim 0.08 \text{ fm}^{-3}$. While the introduction of the κ_q parameters is phenomenological, the gradient terms in

⁵We take the established practice of modelling neutrons and protons with equal masses, i.e. our calculations consistently use $\hbar^2/2m_q = 20.73553 \text{ MeV fm}^2$ for both nucleon species, including in Eq. (18).

the pairing EDF are not without physical motivation: it has long been known that the coupling to collective surface vibration modes leads to an induced pairing-like interaction between nucleons [69], which contributes significantly to mass differences such as $\Delta_{n/p}^{(5)}$ as we will discuss below [70]. Large-scale models relying on a basic mean-field level description of the nucleus cannot directly capture such correlations and thus typically do not distinguish between the bare and induced pairing interaction, especially when attempting to model the effect of both with a simple ansatz such as Eq. (13). Since we aim at deriving here a realistic description of the pairing gaps in INM where surface vibrations are absent, it becomes natural to mock-up the effect of the induced interaction in finite nuclei with the simple gradient term in Eq. (15). The physics of surface vibrations is however not without interest for NSs: in the inner crust superfluid neutrons coexist with nuclear clusters where both the bare and induced pairing interaction contribute.

The use of gradient terms in the pairing channel to mock up such effects was, to the best of our knowledge, first proposed in Ref. [71], incorporated later in what is currently known as the Fayans EDF [72, 73] and investigated in combination with a standard Skyrme EDF in Ref. [34]. The goal of these studies differed from ours: they all aim at an improved reproduction of the odd-even staggering of nuclear charge radii for isotopic chains of spherical nuclei, exploiting the contribution of the neutron pairing terms in Eq. (15) to the proton mean-field potential. A detailed investigation of these terms in view of the reproduction of charge radii during the adjustment of a global model like ours is beyond the scope of this manuscript: we drop all contributions of the pairing terms to the nuclear mean fields, as we did for BSkG1 and BSkG2, see also Sec. 2.3.

In summary, the chief difference with the BSkG1 and BSkG2 models is the form of the function $g_q(\rho_n, \rho_p)$: in Refs. [21, 24] we took the simple and entirely phenomenological standard form corresponding to a mix between so-called “surface” and “volume” pairing. A more technical difference concerns the treatment of the cut-off function: to stay close to the formalism in INM, Eq. (12) only cuts states of high energy, while we employed cutoffs both above and below the Fermi energy for the construction of BSkG1 and BSkG2.

2.2 Numerical set-up, symmetries, shapes and blocking

As for the construction of BSkG1 and BSkG2, we rely on the MOCCa code of Ref. [74] to solve the self-consistent Skyrme-HFB equations quickly and robustly [75].

This tool iterates N_N single-neutron and N_Z single-proton wavefunctions on a three-dimensional cubic mesh with $N_{x/y/z}$ points in each Cartesian direction, equally spaced at a distance dx . Through the use of Lagrange-mesh techniques [76], a modest choice of mesh parameters already leads to an excellent numerical accuracy that is essentially independent of the shape of the nucleus [77]. We fixed $dx = 0.8$ fm in all calculations to guarantee a numerical accuracy on absolute energies on the order of 100 keV [77], but we chose slightly different numbers of mesh points and single-particle wavefunctions depending on the context, as we will describe below.

It turned out that numerical safeguards are crucial in order to solve the self-consistent equations for the form of the Skyrme functional we employ here. The density-dependent terms in Eqs. (6)-(7) give rise to contributions to the nuclear mean-field that are proportional to $\rho_0(\mathbf{r})$ raised to the power $(\alpha-1)$, $(\beta-1)$, $(\gamma-1)$ and even $(\beta-2)$. Even though $\rho_0(\mathbf{r})$ is formally guaranteed to be strictly positive everywhere, our values of α , β and γ are smaller than one and typically lead to numerical problems in regions of the simulation volume where $\rho_0(\mathbf{r})$ is small because of the finite precision of floating point arithmetic. For this reason, we replace all instances of $\rho_0^\nu(\mathbf{r})$ with $\nu < 0$ in the mean fields by $(\rho_0(\mathbf{r}) + \epsilon)^\nu$, where $\epsilon = 10^{-8} \text{ fm}^{-3}$ ⁶.

Another important aspect of our calculations is the self-consistent symmetries imposed on the nuclear configurations: each additional symmetry assumption greatly reduces the computational burden but also removes degrees of freedom that can be relevant to the description of the nucleus. In all calculations, we assume the nuclear configurations to be invariant under the z -signature \hat{R}_z and y -time-simplex \hat{S}_y^T operators [78], such that we were only required to numerically represent one-fourth of the entire simulation volume corresponding to the positive x - and y -axes. Calculations under these conditions are however very demanding even for modest mesh parameters such that, when possible, we further simplified calculations by imposing reflection symmetry, time-reversal symmetry or both as we elaborate below in more detail.

Symmetry assumptions restrict the range of nuclear shapes that can be explored. One way to characterize the latter is the multipole moments $\beta_{\ell m}$ of the nuclear density, that we define exactly as in Ref. [21] for integer $\ell \geq 1$ and integer $0 \leq m \leq \ell$. In our most general

⁶In fact, we also employed this recipe for BSkG1 and BSkG2 with $\epsilon = 10^{-20} \text{ fm}^{-3}$. The additional density dependencies we employ here force us to enlarge the value of ϵ significantly.

⁷We remind the reader that such multipole moments characterize the deformation of the nuclear volume and are for

calculations, all moments $\beta_{\ell m}$ for arbitrary ℓ and even m are allowed to be non-zero. In particular, this includes two quadrupole deformations β_{20} and β_{22} and two octupole deformations β_{30} and β_{32} . For plotting and interpretation purposes, we will also use an equivalent, widely-used, characterization of the quadrupole deformation⁸ in terms of (β_2, γ) :

$$\beta_2 = \sqrt{\beta_{20}^2 + 2\beta_{22}^2}, \quad (20a)$$

$$\gamma = \text{atan}\left(\sqrt{2}\beta_{22}/\beta_{20}\right). \quad (20b)$$

These values characterize the shape of a nucleus and should not to be confused with the exponents of the density-dependent terms in the EDF. Although multipole moments of order $\ell \geq 4$ are less often discussed, they generally do not vanish [21] and can impact both low- and high-energy experiments [42, 80, 81].

All multipole moments that are not restricted by symmetry are naturally included in the self-consistent optimization of the mean-field energy E_{HFB} . The correction energy E_{corr} is however a complicated function that cannot easily be included self-consistently in the Skyrme-HFB equations: as for the previous BSkG models, we include it perturbatively in any given MOCCA calculation but semivariationally optimize the total energy E_{tot} by performing multiple calculations constrained to different values of (β_{20}, β_{22}) [21, 24] to find the nuclear ground state. It would have been prohibitively expensive to extend this two-dimensional search to include β_{30} and/or β_{32} . Instead, we perform a semivariational search in (β_{20}, β_{22}) twice for each nucleus: once with the assumption of reflection symmetry and once without, forcing the nucleus to explore reflection asymmetric degrees of freedom by activating a constraint on a finite value of β_{30} for a few iterations. These searches yield two nuclear configurations (that coincide for many nuclei), from which we select the one with the lowest total energy as our calculated nuclear ground state.

Our semivariational procedure is not completely general: we restricted our calculations to $\gamma \in [0^\circ, 60^\circ]$. The simplest of our calculations respect reflection symmetry and time-reversal symmetry; in this case values of $\gamma > 60^\circ$ reflect different orientations of the nuclear configuration in the simulation volume. Breaking time-reversal symmetry allows the nucleus to develop a finite angular momentum while breaking reflection symmetry allows for finite octupole deformation; both of these

that reason not directly comparable to the deformation parameters typically used in analytical parameterisations of the nuclear density, see the discussion in Ref. [42].

⁸It is entirely possible to similarly recast the octupole deformations β_{30}, β_{32} in terms of an overall size of the octupole deformation β_3 and an associated angle γ_3 [79], but these variables are not widely used.

quantities define a preferred direction in space such that the degeneracy due to the reorientation of the nucleus is partially lifted. We ignore this complexity here entirely for computational reasons, but our restriction to $\gamma \in [0^\circ, 60^\circ]$ is not without physical motivation: (i) reorientation effects due to the presence of angular momenta are small at least for odd-mass nuclei [82] and (ii) our search covers the special case of shapes with $\gamma = 0^\circ$ and finite values of β_{30} that is the subject of virtually all literature on ground state octupole deformation. Nuclear shapes that combine non-axial quadrupole deformation and octupole deformation are relevant to fission [83], but we are not aware of any indication that such shapes are relevant to nuclear ground states.

In typical conditions, the Bogoliubov many-body state with the lowest energy for a fixed configuration of the nuclear mean fields will have even number parity for both protons and neutrons. To correctly describe the physics of the unpaired nucleons, we excite one or two quasiparticle excitations with respect to this lowest state when describing odd-mass or odd-odd nuclei, respectively. We employ the gradient solver strategy briefly described in Ref. [83] to facilitate these calculations and to guarantee we obtain the state of lowest energy at convergence. To limit the computational effort, we consider only quasi-particle excitations with z -signature quantum number $+i$ which slightly limits the generality of our calculations for odd-odd nuclei but is sufficient for odd-mass systems [83]. As for BSkG1 and BSkG2, allowing for triaxial deformation implies that we cannot cleanly associate rotational quantum numbers with the ground-states of odd-mass and odd-odd nuclei. When breaking reflection symmetry, we can no longer associate a parity quantum number with these states either. Remedying these defects of our model would require very expensive symmetry-restoration techniques, whose systematic application to large numbers of nuclei is not feasible today.

Having clarified these general aspects of our approach, we are now in a position to describe in detail the three types of calculations we performed during this work: (i) calculations targeting ground states during the parameter adjustment, (ii) calculations targeting ground states to build the final table of results, after the parameter adjustment and (iii) calculations targeting fission barriers.

Ground state calculations during the fit To save on computational resources, we took $N_x = N_y = N_z = 32$ and iterated only $N_N = N + 160$ and $N_Z = Z + 100$ single-particle states during the fit for a nucleus with N neutrons and Z protons [21]. For even-even nuclei we assume time-reversal but we did not do so for odd-mass

or odd-odd systems. We impose reflection symmetry for all calculations, which allowed us to further reduce the numerical representation to just one-eighth of the entire simulation volume. We emphasize that we did not include the possibility of octupole deformation in the parameter adjustment, which is justified a posteriori by the limited number of nuclei affected.

Final ground state calculations: To make sure the final results are well converged with respect to all numerical parameters, our final calculations employed $N_x = N_y = N_z = 36$ mesh points in each Cartesian direction and $N_N = N + 400$ and $N_Z = Z + 240$ single-particle states. As during the parameter adjustment, we only assume time-reversal invariance for even-even nuclei. We did not assume reflection symmetry, giving a priori all nuclei the freedom to use octupole deformation to lower their total energy according to our search strategy explained above.

Fission calculations: To obtain the static fission properties of the actinide nuclei included in the fit protocol, see Sec. 3, we followed the procedure detailed in Ref. [83]; we repeat here only a few essential points. We take the two quadrupole deformations as collective variables and construct two-dimensional potential energy surfaces (PES) through repeated calculations constrained to different values of (β_{20}, β_{22}) . In each of these calculations, we take $N_x = N_y = 32$, $N_z = 40$ mesh points to accommodate the elongated shapes relevant to fission and iterate only $N_N = 440$ and $N_Z = 260$ states; these choices certainly limit our accuracy with respect to the total energy but still allow for a numerical accuracy of roughly 100 keV for energy differences such as the barriers and isomer excitation energies. We established in Ref. [83] that the effect of time-reversal symmetry breaking on such static fission properties is small and, for this reason, assume conservation of time-reversal symmetry in all fission calculations, employing the equal-filling-approximation in the case of odd-mass and odd-odd nuclei to account for the blocking effect of odd nucleon(s) [84]. To reduce the computational burden, we assume reflection symmetry for nuclear configurations with $\beta_{20} < 1$. We relax this restriction at larger deformations, as the actinide nuclei we consider here typically exploit octupole deformation to lower their energy at deformation above $\beta_{20} \approx 1$ [83]. From the PES thus constructed, we used a flooding model to determine the lowest energy fission path (LEP) connecting the ground state with a fissioned system. We obtain through interpolation the excitation energy of the local maxima along this path, which by construction are saddle points on the two-dimensional PES. It is these excitation energies that we compare to the empirical values

listed in the RIPL-3 database [85]. A final remark concerns nomenclature: it is natural to discuss the inner and outer barrier for actinide nuclei corresponding to the local maxima along the LEP encountered at moderate and large deformation. Experimental information is not sensitive to the ordering of barriers in terms of deformation, such that we discuss all results in terms of the primary (highest) and secondary (lowest) barriers.

2.3 BSkG versus BSk model ingredients

All terms of the functional underlying BSkG1 and BSkG2 are essentially standard. With the extensions discussed in the preceding subsections, the new BSkG3 model has now reached parity with the last entries in the BSk-model series [23] in terms of the formal properties of all relevant equations. Among the BSkG-models, BSkG3 is thus the most directly comparable to BSk30, BSk31 and BSk32. Several differences nevertheless remain, primarily due to the different numerical set-up as discussed in detail in Ref. [21]: the three-dimensional coordinate representation gives the BSkG models (i) an extended reach in terms of the symmetries imposed on the nuclear configuration, (ii) an improved numerical accuracy but also (iii) a different discretisation of single-particle states in the continuum, and hence, pairing properties when compared to the BSk-models. Not all aspects of pairing are necessarily different, however: intriguingly, mass fits that account for pairing self-energy result naturally in low values of the pairing cutoff: $E_{\text{cut}} = 6.5$ MeV for BSk30-31-32 [23]. This is the natural size for coordinate space implementations such as ours, but this value is several times smaller than the cutoffs typically employed with numerical implementations that rely on an expansion in terms of harmonic oscillator basis states. Low values of the cutoff also arise naturally if one requires the pairing terms in the limit of $\rho \rightarrow 0$ to be compatible with the experimental neutron-neutron 1S_0 scattering length, see the discussion in Refs. [68, 86, 87].

Other than those due to the numerical representation, there remain four minor differences that separate BSkG3 from BSk30-31-32. First is the precise role of the parameters κ_q : since in Ref. [23] these determined the size of the pairing terms involving gradients in an absolute sense, while here they get multiplied by the deduced $V_q(\rho_n, \rho_p)$. The result is that the values of these parameters for the BSk30-31-32 models are not directly comparable to the ones we obtain here. Contrary to the older models, the form of Eq. (15) ensures that all pairing terms are consistently renormalized when the value of E_{cut} is changed. With this feature, our new EDF now becomes more suitable for time-dependent HFB calculations: only with much larger cutoff values can one re-

liably follow the dynamical evolution on the timescales relevant to applications, see Refs. [88, 89]. Aside from their relevance to the description of reactions of finite nuclei and nuclear fission in particular [90–92], such approaches are also of interest to explore various phenomena in NSs, for instance, the dynamics of neutron superfluid vortices in the crust [93].

Second, all BSk models starting from the very first [22] manually enlarge the pairing strength by about 5% for nucleon species $q = p, n$ when the corresponding particle number N_q is odd. For BSk30-31-32, this is accomplished through parameters $f_q^+ = 1$ and $f_q^- \approx 1.05$ that multiply $g_q(\rho_n, \rho_p)$ in the equivalent of Eq. (11) in Ref. [23] when N_q is even or odd, respectively. This recipe was formally motivated in Ref. [94] as a phenomenological way to (i) account for time-reversal symmetry breaking and (ii) the residual interaction between the odd neutron and odd proton in odd-odd nuclei and led in practice to improved mass fits. We have opted not to employ this recipe for several reasons. First, the factors f_q^\pm cannot directly be linked to an effective interaction. Second, we now explicitly account for time-reversal symmetry breaking as we did with BSkG2. Third, we have recently shown that BSk31, BSkG1 and BSkG2 all fail to describe the global trends of $\Delta_{np}^{(3)}$, specific mass differences that are linked to the residual np -interaction in odd-odd nuclei [95]. The evidence of Ref. [94] and the BSk-models indicates that including the f_q^\pm factors does lead to somewhat improved mass fits, but at the cost of two additional parameters that are entirely phenomenological in nature: we prefer not to include them here for the sake of predictive power. We defer to a future study the investigation of more microscopic ways to reproduce at least qualitatively the $\Delta_{np}^{(3)}$ mass differences and make up the difference in rms deviation of the masses globally.

Third, our recipe to extend the INM pairing gaps to arbitrary values of asymmetry δ is different than that employed for BSk30-31-32. During the initial phases of this work, we discovered a flaw in the recipe of Ref. [23]: it leads to negative pairing gaps when $|\delta|$ is large but not equal to 1. Our new choice, Eq. (14), is guaranteed to produce strictly positive values of the pairing gaps for both nucleon species for all values of δ .

A final difference concerns our treatment of the mean-field potentials: as $g_q(\rho_n, \rho_p)$ depends on the nucleon densities, the pairing terms of the EDF in Eq. (11) should contribute to the mean-field potentials, see for instance the appendix of Ref. [51]. We neglect here this coupling between the pairing and particle-hole parts of the EDF for simplicity, as we did for BSkG1 and BSkG2.

3 Optimization procedure

The new model is formulated in terms of 29 parameters of which seventeen are related to the Skyrme functional, three to the pairing functional (κ_n, κ_p , and E_{cut}), five to the collective correction ($b, c, d, l, \beta_{\text{vib}}$) and four to the Wigner energy (V_W, λ, V'_W and A_0)⁹. BSkG2 relied on 25 parameters; the new model adds six new parameters that characterize the additional terms in the Skyrme functional ($t_4, t_5, x_4, x_5, \beta, \gamma$) parameters and two new pairing parameters (κ_p, κ_n) but no longer includes four parameters ($V_{\pi n}, V_{\pi p}, \eta, \xi$) that specified the more phenomenological pairing terms of the preceding model.

The primary ingredient of the objective function of our parameter adjustment is the set of 2457 experimental nuclear atomic masses with $Z \geq 8$ from AME20 [60]. Adjusting 29 parameters on thousands of data points that all require at least one MOCCA calculation would be infeasible if approached naively. Here, we rely again on the machine learning techniques developed for the adjustment of BSkG1 [21]: we train several Multi-Layer Neural Networks (MLNNs) to serve as emulators of MOCCA. A growing library of MOCCA calculations serves to train the members of the committee, which then jointly predict new parameter values of increased fitness that serve for further training. Once we reach an optimal set of parameter values, we perform complete calculations with MOCCA to obtain all the results we discuss below. We emphasize that we employ the MLNNs solely as a way to accelerate the parameter adjustment; the resulting model relies in no way on interpolation or extrapolation through machine learning.

Aside from the known masses, we also fit the average pairing gaps $\langle uv\Delta \rangle_q$ ($q = p, n$) to experimental values of the five-point neutron and proton gaps $\Delta_q^{(5)}$ for nuclei that are sufficiently far from the spherical shell closures [21, 57]. We include these quantities in the objective function¹⁰ to control the overall size of the pairing parameters κ_n and κ_p , since a fit to only the masses tends to produce unrealistically large pairing strengths that would deteriorate the quality of our model for other observables [96]. In this respect, the approach we adopt here for the pairing parameters differs from that used for BSkG2 in two ways. First, we now control the neutron and proton pairing strengths as opposed to just the neutron one. Second, we do not fit the proton gaps of odd- Z isotopic chains nor the neu-

⁹For completeness, we detail the way the Skyrme functional depends on these parameters in Appendix B and provide formulas for the rotational and vibrational correction as well as the Wigner energy in Appendix C.

¹⁰We include the pairing gaps in the objective function with a weight of 19% relative to the absolute values of the masses.

tron gaps of odd- N isotonic chains: the $\Delta_q^{(5)}$ along such chains involve the binding energy of odd-odd nuclei and are for that reason systematically smaller than the gaps in neighbouring even- Z or even- N chains. This leaves the objective function with 957 and 1153 experimental values for $\Delta_p^{(5)}$ and $\Delta_n^{(5)}$, respectively. As discussed briefly in Sec. 2.3, current large-scale microscopic mass models do not account for this effect [95,97]. Pending a dedicated study, we prefer to remove the affected mass differences from the objective function in order to not contaminate the final parameter set.

To include the physics of large deformation in general and fission in particular, we employ the two-step procedure that was originally devised for BSk14 and that we employed for BSkG2 [24,83,98]. We repeat here only the key points: we perform an initial fit that includes only experimental information on ground state properties. Using the optimal parameter values resulting from this first step, we calculate fission barriers and isomeric excitation energies as outlined in Sec. 2.2. Freezing all other parameters, we continue fitting in a second step the nine parameters of the collective correction to reproduce at best, simultaneously, ground state properties, the RIPL-3 empirical barriers, and the known isomeric excitation energies. For BSkG2, we limited this fit to twelve even-even nuclei; with the experience of Ref. [83] under our belts, we now include the barriers of all 45 nuclei with $Z \geq 90$ that are listed in RIPL-3 as well as their 28 known isomeric excitation energies [99].

At all stages of the parameter adjustment, we control the INM properties of the parameterisation in several ways. First, we fix several of the INM properties at saturation density: we set the symmetry energy coefficient $J = 31$ MeV and we restrict the incompressibility modulus K_v and the isoscalar effective mass M_s^*/M to the intervals [230, 250] MeV [100] and [0.8, 0.86] [101], respectively. We also adjust k_F to reproduce the global trend of known charge radii. The spirit of these choices is identical to the ones made for BSkG1 and BSkG2, but our value of J is different. We set $J^{\text{BSkG1}/2} = 32$ MeV before by the desire to have a NeutM EoS with some minimal degree of stiffness, though this did not suffice to render the previous models consistent with the existence of heavy pulsars. For the extended Skyrme form we employ here, this constraint no longer applies and $J = 31$ MeV was shown to be close to optimal for the global description of masses and particularly well-suited to reproduce the binding energies of neutron-rich nuclei in Ref. [23]. We confirmed this with exploratory calculations, but did not consistently include J as a free parameter in the optimization. Our control of K_v was facilitated by our choice of the exponents of the various

density dependencies: the parameters α, β and γ were chosen as in Ref. [23] and were not actively adjusted.

A second aspect of control is new: we restrict the energy of NeutM at $\rho = 1 \text{ fm}^{-3}$, i.e. at high density prevailing in NS cores, to the interval [550, 600] MeV, ensuring in this way a sufficiently stiff EoS and hence the compatibility of our model with the existence of pulsars with masses above $2M_\odot$.

In summary, the objective function and the parameter adjustment strategy of BSkG3 are similar but not identical to those of BSkG2 [24]. The differences are: (i) the inclusion of proton pairing gaps but removal of neutron (proton) pairing gaps along odd- Z isotopic (odd- N isotonic) chains, (ii) a larger selection of fission data that now also encompasses odd-mass and odd-odd nuclei and (iii) added a constraint on the energy of NeutM at high density.

4 Properties of atomic nuclei

4.1 The BSkG3 parameterisation

Table 1 contains the values of all 29 parameters that characterize the BSkG3 model: the first group of 17 parameters determines the Skyrme part of the functional, the second group consists of 3 parameters specifying the pairing terms, the third group of 5 parameters and the final group of four parameters governs the collective correction and the Wigner energy, respectively. For comparison, Table 1 also contains all parameter values of BSkG2 [24], although four of its pairing parameters ($V_{\pi n}$, $V_{\pi p}$, η and ξ) do not have a counterpart in the new model.

Table 2 showcases the global performance of the model for atomic nuclei. Concerning ground state properties, it lists the mean ($\bar{\epsilon}$) and rms (σ) deviations of the model with respect to all 2457 known masses of nuclei with $N, Z \geq 8$ in AME20, as well as the known neutron separation energies and β -decay energies from the same mass evaluation and 810 known charge radii from Ref. [102]¹¹. We also show the mean and rms deviations with respect to 45, i.e. all reference values with $Z \geq 90$ from the RIPL-3 database [85] for the primary (E_I) and secondary (E_{II}) barriers. Finally, the table lists the deviations for the subset of 28 actinide nuclei for which the excitation energy of a fission isomer (E_{iso}) is known.

BSkG3 presents a modestly (though not negligible) improved description over BSkG2 for ground-state properties: the rms deviation for the known masses and

¹¹Note that only 810 experimental charge radii in Ref. [102] are considered here, excluding their Re, Po, Rn, Fr, Ra, Am and Cm values derived from systematics.

Table 1 The BSkG3 parameter set: seventeen parameters determining the self-consistent mean-field energy E_{HFB} , three to the pairing functional, and nine determining the correction energy E_{corr} . For comparison, we include the values of the BSkG2 parameter set [24]. Note that instead of parameter x_2 we list the values of the product $x_2 t_2$.

Parameters	BSkG2	BSkG3
t_0 [MeV fm ³]	-1885.74	-2325.35
t_1 [MeV fm ⁵]	343.59	749.82
t_2 [MeV fm ⁵]	-8.04132	0.01
t_3 [MeV fm ^{3+3α}]	12358.4	14083.45
t_4 [MeV fm ^{5+3β}]		-498.01
t_5 [MeV fm ^{5+3γ}]		266.52
x_0	0.181775	0.558834
x_1	-0.584003	2.940880
$x_2 t_2$ [MeV fm ⁵]	-162.003	-432.256954
x_3	0.101596	0.628699
x_4		5.657990
x_5		0.396933
W_0 [MeV fm ⁵]	108.655	119.735
W'_0 [MeV fm ⁵]	108.603	78.988
α	0.3	1/5
β		1/12
γ		1/4
$V_{\pi n}$ [MeV]	-483.366	
$V_{\pi p}$ [MeV]	-503.790	
η	0.486	
ξ	0.796	
κ_n [fm ⁸]		123.20
κ_p [fm ⁸]		129.07
E_{cut} [MeV]	7.998	7.961
b	0.878	0.810
c	8.293	7.756
d	0.595	0.289
l	4.555	5.499
β_{vib}	0.788	0.827
V_W [MeV]	-1.805	-1.716
λ	252.17	437.20
V'_W [MeV]	0.745	0.502
A_0	35.496	37.801

charge radii is, respectively, 6% and 12% smaller than its predecessor. The global improvements for the S_n and Q_β values amount to roughly 12% and 15%, respectively. This is not a trivial observation, since an improved description of the absolute values of the masses does not guarantee a reduced rms deviation for mass differences. Since the BSkG3 model ingredients differ in several ways from the BSkG2 ones, it is not possible to unambiguously pinpoint a single source for this improvement. Nevertheless, we note that both the microscopic treatment of pairing [104], and the reduced value of J [23] have shown to lead to a reduction of the rms deviation on the masses in the past.

The description of known absolute binding energies that BSkG3 offers does not quite reach the level of the later entries in the BSk-series; in particular BSk27 achieves an rms deviation of 0.512 MeV with respect

Table 2 Root-mean-square (σ) and mean ($\bar{\epsilon}$) deviations between experiment and predictions for the BSkG2 and BSkG3 models. The first block refers to the nuclear ground-state properties and the second one to fission properties. More specifically, these values were calculated with respect to 2457 known masses (M) [60] of nuclei with $Z, N \geq 8$, the subset of 299 known masses M_{nr} of neutron-rich nuclei with $S_n \leq 5$ MeV, 2309 neutron separation energies (S_n), 2173 β -decay energies (Q_β), 810 measured charge radii (R_c) [102], 45 empirical values for primary (E_{I}) and secondary (E_{II}) fission barrier heights [85] and 28 fission isomer excitation energies (E_{iso}) of actinide nuclei [99]. The first line gives the model error [103] on all the measured masses.

Results	BSkG2	BSkG3
$\sigma_{\text{mod}}(M)$ [MeV]	0.668	0.627
$\sigma(M)$ [MeV]	0.678	0.631
$\bar{\epsilon}(M)$ [MeV]	+0.026	+0.080
$\sigma(M_{nr})$ [MeV]	0.851	0.660
$\bar{\epsilon}(M_{nr})$ [MeV]	+0.308	-0.011
$\sigma(S_n)$ [MeV]	0.500	0.442
$\bar{\epsilon}(S_n)$ [MeV]	-0.006	+0.009
$\sigma(Q_\beta)$ [MeV]	0.619	0.534
$\bar{\epsilon}(Q_\beta)$ [MeV]	-0.019	+0.021
$\sigma(R_c)$ [fm]	0.0265	0.0237
$\bar{\epsilon}(R_c)$ [fm]	+0.0007	+0.0006
$\sigma(E_{\text{I}})$ [MeV]	0.44	0.33
$\bar{\epsilon}(E_{\text{I}})$ [MeV]	+0.24	+0.06
$\sigma(E_{\text{II}})$ [MeV]	0.47	0.51
$\bar{\epsilon}(E_{\text{II}})$ [MeV]	+0.10	+0.01
$\sigma(E_{\text{iso}})$ [MeV]	0.49	0.36
$\bar{\epsilon}(E_{\text{iso}})$ [MeV]	-0.36	-0.05

to the AME20 masses [105]. BSk27 is based on a standard Skyrme form and, like BSkG1 and BSkG2, is not compatible with the existence of heavy pulsars. Later models such as BSk31 ($\sigma(M) = 0.585$ MeV) are less accurate but satisfy this constraint. BSkG3 and BSk31 share (almost) all model ingredients such that a comparison between both parameterisations is more direct. The difference in rms deviation between BSkG3 and BSk31 is but a few tens of keV, i.e. roughly 8%, but still significant. Without additional costly parameter fits, we cannot pinpoint the exact origin of this difference but we surmise it is mostly due to our omission of the phenomenological pairing factors $f_{p/n}^\pm$ employed by the BSk-series as discussed in Sec. 2.3. However, when concentrating on the subset of 299 masses of neutron-rich nuclei with $S_n \leq 5$ MeV (of particular interest for the extrapolation towards the exotic neutron-rich nuclei involved in the r -process nucleosynthesis), the superiority of the BSkG3 model with respect to BSkG2 is striking, with a reduction of about 200 keV. The BSkG3 predictions for this subset also appear to be more accurate than those obtained with BSk27 ($\sigma(M_{nr}) = 0.685$ MeV) and BSk31 ($\sigma(M_{nr}) = 0.733$ MeV). When dealing with mass differences, BSkG3 describes the S_n and Q_β values

with accuracy rather similar to (or even better than) the one found by the latest BSk models, in particular $\sigma(S_n) = 0.429$ MeV and 0.479 MeV and $\sigma(Q_\beta) = 0.525$ MeV and 0.597 MeV, for BSk27 and BSk31, respectively.

We argued in Ref. [83] that BSkG2 offered the best all-round global description of static fission properties: its simultaneous description of primary and secondary barriers, as well as isomeric excitation energies of the 45 $Z \geq 90$ actinide nuclei with an rms deviation of less than 0.500 MeV was unmatched in the literature at the time of writing. However, the new BSkG3 model does significantly better in several ways. First, the primary fission barriers, which remain the most important quantity from the point of view of applications, are reproduced with an rms deviation of only 0.330 MeV, i.e. a reduction of 25% compared to BSkG2. Only the PC-PK1 [106] model outperforms BSkG2 in describing primary barriers: it achieves an rms deviation of 0.37 MeV but results are only available for twelve even-even nuclei. The rms deviation of BSkG3 for primary barriers is, to the best of our knowledge, the lowest ever reported in the literature. Also, the rms deviation for fission isomers has decreased by a similar amount. Second, the mean deviations $\bar{\epsilon}$ have been reduced dramatically for all three fission properties: a factor of two for the secondary barriers, four for the primary barriers and even nine for the isomer excitation energies. The only (minor) downside is a slightly larger rms deviation for the secondary barriers: $\sigma(E_{II}) = 0.51$ MeV. We will discuss the BSkG3 fission properties and the reasons for this improved performance in more detail in Sec. 4.6, but mention already here that it is not due to the incorporation of additional parameters related to fission.

We end this discussion of global performance with a remark on the neutron skin of ^{208}Pb , which the new model predicts to be 0.16 fm, a value somewhat smaller than the value obtained with BSkG1 and BSkG2 (0.18 fm). This is as expected from our choice to implement a lower symmetry energy coefficient J compared to the preceding models. Both values remain in good agreement with constraints deduced from measurements of the electric dipole polarisability [107], the antiproton capture of ^{208}Pb [108], and ab-initio predictions [14]. The authors of Ref. [109] have recently derived the ^{208}Pb neutron skin from ultrarelativistic heavy collision of $^{208}\text{Pb} + ^{208}\text{Pb}$. They obtain $\Delta r_{\text{np}} = 0.217 \pm 0.058$ fm, our prediction is therefore marginally consistent within the lower limit of this result. Nonetheless, BSkG1-3 predictions differ from the value of 0.283 ± 0.071 fm reported by the PREX-II collaboration [110] extracted from measurements of the parity-violating asymmetry in the elastic scattering of longitudinally polarized elec-

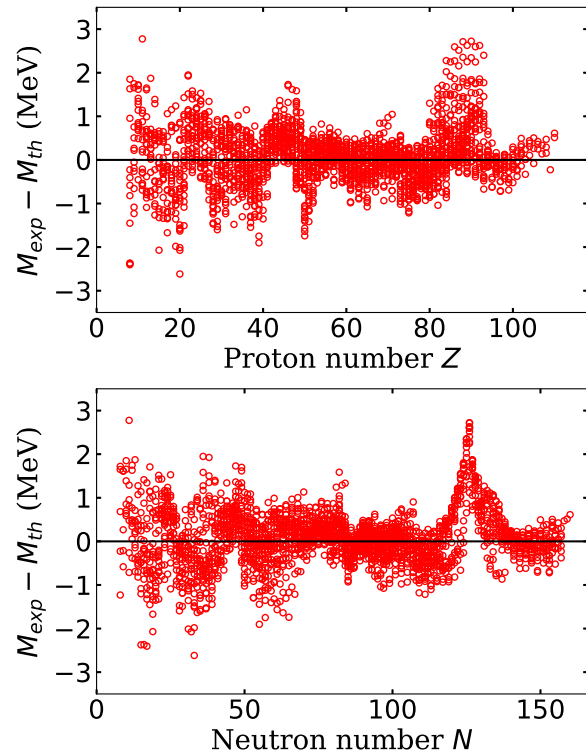


Fig. 2 Differences between experimental [60] and BSkG3 masses as a function of the proton number (top) and neutron number (bottom).

trons on ^{208}Pb . The PREX-II value remains noticeably larger than those derived from the above-mentioned experiments and from theoretical predictions.

4.2 Nuclear masses

We show the difference between experimental and calculated masses in Fig. 2 as a function of proton number (top panel) and neutron number (bottom panel). The BSkG3 model achieves a general good fit to the data with only a few nuclei exhibiting a deviation that is larger than 2 MeV. The largest deviations concern either light nuclei or nuclei close to the magic numbers; these patterns are similar to those of BSkG- and BSk-families of models [23, 24].

In Fig. 3 the difference between the masses obtained with BSkG3 and BSkG2 (top) or BSk31 (bottom) are displayed as a function of the neutron number for all nuclei with $8 \leq Z \leq 118$ lying between the BSkG3 proton and neutron drip lines. We note that BSkG3 produces binding energies that are, on average, smaller than the ones obtained from BSkG2 for intermediate and light nuclei. For heavy nuclei BSkG3 obtains binding energies predominantly larger than BSkG2. These differ-

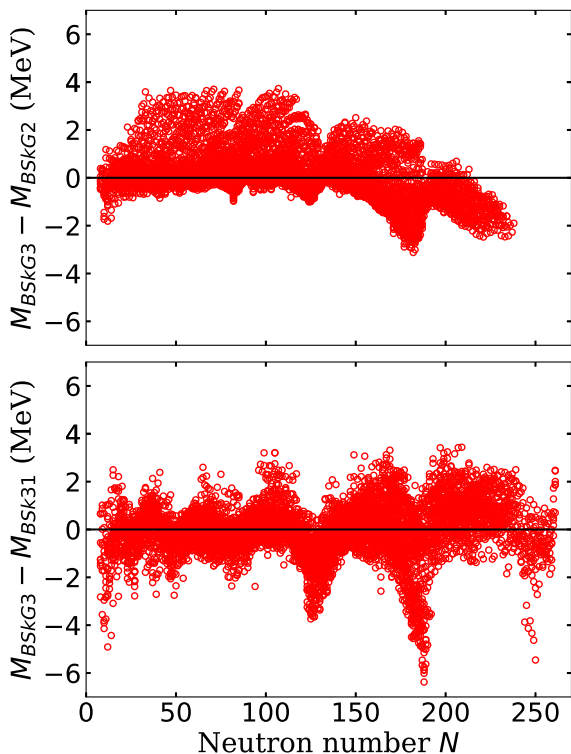


Fig. 3 Mass differences between BSkG3 and BSkG2 [24](top) and BSkG3 and BSk31 [23](bottom) as a function of the neutron number N for all nuclei with $8 \leq Z \leq 118$ lying between the BSkG3 proton and neutron drip lines.

ences are rather smooth, due to the similar predictions for shell gaps among BSkG2 and BSkG3, as noted in Fig. 4. These differences, however, never exceed 4 MeV. When compared to BSk31 we note a larger difference between models, especially close to the $N = 126$ and $N = 184$ shell closures where it can reach up to 6 MeV. This can be understood from the stronger shell effects for this model (see Fig. 4) which is a consequence of the lower isoscalar effective mass of BSk31, as seen in Tab. 3.

4.3 Shell structure

The shell effects can be investigated by the neutron and proton shell gaps defined as,

$$\delta_{2n}(N_0, Z) = S_{2n}(N_0, Z) - S_{2n}(N_0 + 2, Z), \quad (21)$$

$$\delta_{2p}(N, Z_0) = S_{2p}(N, Z_0) - S_{2p}(N, Z_0 + 2), \quad (22)$$

where $S_{2n/p}$ are the two-neutron/-proton separation energies. The $\delta_{2n/p}$ are indicators for shell closures, but they are not measures of the size of the gap in the single-particle spectrum as they are sensitive to any structural change between the three nuclei entering Eqs. (21-22) [111].

We show in Fig. 4 the $\delta_{2n/p}$ values across spherical shell closures for the BSkG2, BSkG3 and BSk31 models for the chains of heavy semi-magic nuclei, as well as available experimental data. All three models produce similar neutron shell gaps for the $N_0 = 50$ and 82 gaps, agreeing with experimental values about equally well. We note that for $N_0 = 126$ (upper middle), BSk31 predicts smaller shell gaps for $68 < Z < 82$ with stronger odd-even staggering in comparison to BSkG2 and BSkG3. The bottom middle panel shows the neutron gap near $N_0 = 184$ where, for the neutron rich isotopes, BSk31 produces a gap roughly 13% higher than BSkG2 and BSkG3, while the three models agree with each other for $Z > 82$. For $Z_0 = 50$ (upper right), BSk31 predicts stronger proton gaps for $N > 82$, reaching $\approx 25\%$ around $N = 88$. For the $Z_0 = 82$ proton shell gap (bottom right), BSk31 produces a $\approx 15\%$ higher gap around $N = 126$, and even a stronger gap for the most neutron rich isotopes around $N \geq 166$. The difference between the BSk31 and BSkG3 shell gaps explains the large mass differences at $N \approx 126$ and $N \approx 184$ in Fig. 3. Despite a relatively good overall agreement between experimental and BSkG3 shell gaps, the $N_0 = 126$ neutron shell gaps remain overestimated leading to an overbinding of masses along the ^{208}Pb isotonic chain, as clearly observed in Fig. 3. This shell gap was better described by some of the BSk models, in particular BSk27 [105].

4.4 Pairing properties

The right (left) panels of Fig. 5 show the five-point neutron (proton) gaps $\Delta_{n/p}^{(5)}$ for BSkG3, BSkG2, BSk31 and available data. The top left panel shows $\Delta_n^{(5)}$ for Zr ($Z = 40$), bottom left for Pb ($Z = 82$) while right panels shows the $\Delta_p^{(5)}$ for the isotones $N = 62$ (top) and $N = 120$ (bottom). This quantity is generally indicative of the strength of pairing correlations in nuclei, but other effects such as time-odd terms (see discussion in Ref. [95]) and structural changes along isotopic chains also contribute [112]. The models predict overall similar $\Delta_{n/p}^{(5)}$ and reproduce rather well the experimental values. A few differences are however present. On top left ($Z = 40$) we note that BSkG2 and BSkG3 underestimate the neutron pairing gaps for neutron-deficient nuclei, and BSk31 reproduces better the experimental data in this particular region. For $Z = 82$ all models present similar predictions for the neutron-deficient region and close to the $N = 126$ shell closure. For the neutron-rich region, beyond $N = 126$, BSk31 presents lower values for the neutron pairing gaps when compared to BSkG's, in particular in the region $N \approx 138$

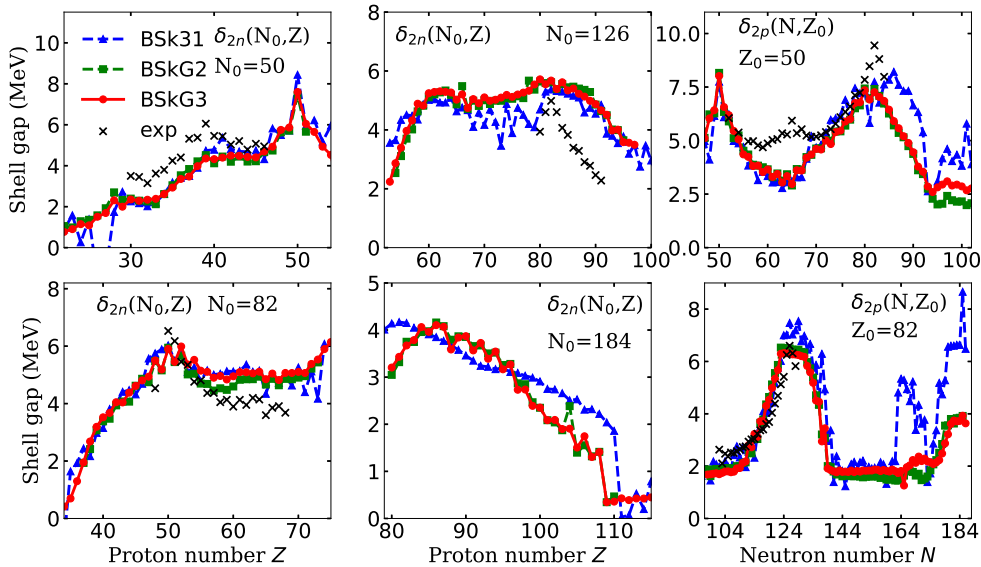


Fig. 4 Shell gaps predicted by BSk31 (blue triangles), BSkG2 (green squares) and BSkG3 (red circles) for $N=50$, $N=82$, $N=126$, $N=184$, $Z=50$ and $Z=82$. Results are compared with available data from AME20 [60] (black crosses).

where $\Delta_n^{(5)}$ is close to zero. Finally, for $N = 120$ all models reproduce rather well the experimental data, they however present considerable differences in the proton-deficient region where BSk31 predicts significantly lower values for the proton pairing gaps compared to BSkG2 and BSkG3. This is directly related to the interpolation recipe used to compute pairing gaps from INM at arbitrary asymmetry values: BSk31 systematically predicts a collapse of the $\Delta_p^{(5)}$ for proton-deficient nuclei. Our new prescription (see Eq. (14) and Sec. 2.3) avoids such a collapse for extreme N/Z values.

The rotational moment of inertia is another way to gauge the pairing properties of the new model. We compare in Fig. 6 the calculated Belyaev moments of inertia (MOI) to experimental data for 48 even-even nuclei [113–115]. Although the Belyaev MOI is a crucial ingredient in the collective correction, Eq. (3), it remains a perturbative quantity that does not capture all aspects of the nuclear response to rotation. A more advanced calculation results in values roughly 32% larger [24]: we show for simplicity all calculated values multiplied with 1.32. With this simple correction taken into account, both BSkG2 and BSkG3 reproduce fairly well the experimental values for medium-heavy nuclei, indicating that the pairing properties of BSkG3 were also well-controlled in this respect. We observe though that BSkG2 produces somewhat larger MOI values in this region. All BSkG models, including BSkG1 (not shown) underestimate systematically the MOI of actinide nuclei, although it is unlikely that pairing properties are the culprit.

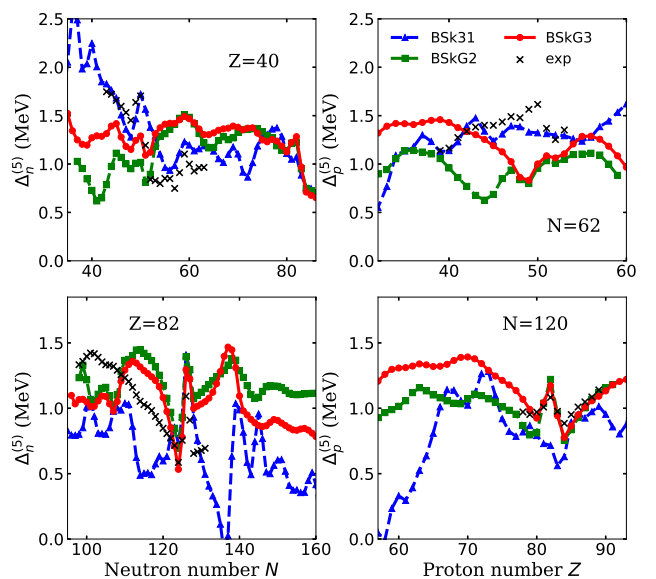


Fig. 5 Left: Neutron five-point pairing gaps $\Delta_n^{(5)}$ along the Sn(top) and Pb(bottom) isotopic chains as calculated with BSkG3 (red circles), BSkG2 (green squares) and BSk31 (blue triangles). Right: Proton five-point pairing gaps $\Delta_p^{(5)}$ along the $N=82$ (top) and $N=120$ (bottom) isotonic chains. Black crosses show the experimental data from AME20 [60].

4.5 Ground state deformations

Our three-dimensional numerical representation naturally allows the nuclear ground state densities to adopt a wide range of deformed, i.e. non-spherically symmetric, shapes that can be characterized by the multipole moments $\beta_{\ell m}$. In practice, we find five qualitatively different types of shapes: (i) rotationally symmetric spheres

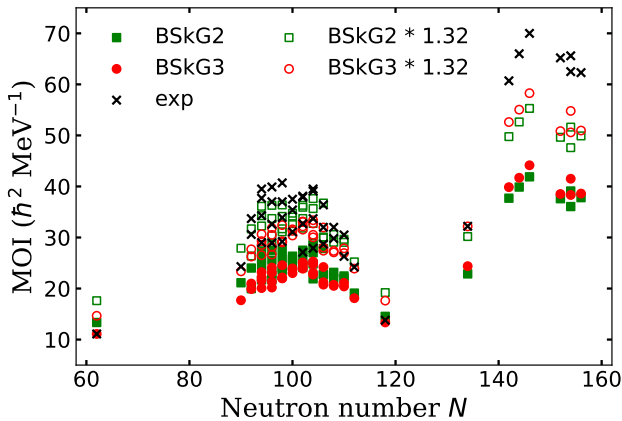


Fig. 6 Belyaev moments of inertia (MOI) as a function of neutron number for BSkG2 (green squares) and BSkG3 (red circles). Experimental data [113–115] is given in black squares. See text for details.

($\beta_{\ell m} = 0$ for all ℓ, m) (ii) axially symmetric ellipsoids ($\beta_2 > 0, \beta_3 = 0$) that are either prolate ($\gamma = 0^\circ$) or oblate ($\gamma = 60^\circ$), (iii) triaxial ellipsoids without any rotational symmetry ($\beta_2 > 0, \beta_3 = 0, \gamma \in]0^\circ, 60^\circ[$) (iv) reflection-asymmetric but (nearly) axially symmetric pear-like shapes ($\beta_2 > 0, \beta_3 > 0, \gamma \approx 0^\circ$)¹² and (v) a very limited number of more general shapes that combine triaxial deformation and reflection asymmetry. Although this categorisation gives an intuitive picture of the shapes encountered in our calculations, it is imprecise and incomplete: we repeat our remark of Sec. 2.2 that all multipole moments that are not constrained by imposed symmetries are naturally included in the (semi-)variational optimization of the energy. Although less important than quadrupole deformation, our calculations predict non-vanishing values for both β_4 and β_6 for many nuclei [21]. The multipole moment β_{32} , although allowed in our calculations, is seemingly not meaningfully exploited by any nucleus; we comment on this remarkable absence below.

We already discussed in detail the systematics of quadrupole deformation, both axial and triaxial, in Ref. [21] while its right panel indicates where finite values of β_{30} occur (current) experimental reach. The rms deviation on the masses is thus mostly unaffected by the inclusion of octupole deformation: an artificial BSkG3 mass table restricted to reflection symmetric ground states produces $\sigma_{\text{refl. symm.}}(M) = 0.620$ MeV, only 11 keV lower than our complete calculation and thus justifying a poster-

¹²Although, fruit-wise, these shapes have been said to resemble mangoes more.

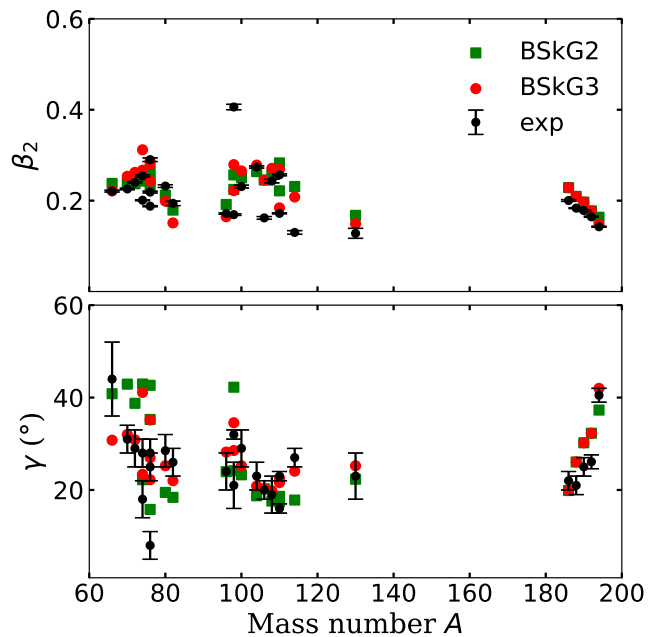


Fig. 7 Calculated quadrupole deformation β_2 (top panel) and triaxiality angle γ (bottom panel) with BSkG2 (green squares) and BSkG3 (red circles), compared to experimental information (black circles with error bars). Top panel: quadrupole deformation β_2 with experimental information from Nudat [116]. Bottom panel: triaxiality angle γ with experimental data points extracted from measured sets of transitional and diagonal $E2$ matrix elements [117–134].

total quadrupole deformation and to mean values of the triaxiality angle obtained from Coulomb excitation experiments [117–134]. Compared to BSkG2, BSkG3 yields nearly identical results for the total quadrupole deformation across this range of mass number A and yet provides a moderately improved description of the triaxiality angle γ for the lightest nuclei with the exception of ^{66}Zn , the lightest isotope in the list.

The possibility of reflection-asymmetric ground states is new to BSkG3: we show its global impact in Fig. 8: its right panel indicates where finite values of β_{30} occur (current) experimental reach. The rms deviation on the masses is thus mostly unaffected by the inclusion of octupole deformation: an artificial BSkG3 mass table restricted to reflection symmetric ground states produces $\sigma_{\text{refl. symm.}}(M) = 0.620$ MeV, only 11 keV lower than our complete calculation and thus justifying a poster-

our choice to not include this degree of freedom in the parameter adjustment.

Octupole deformation becomes energetically favourable when the nucleus has the freedom to mix the single-particle states of a unique-parity intruder shell of angular momentum j with those of a normal-parity $j - 3$ shell [135]. This explains the distribution of octupole deformation in Fig. 8: such single-particle configurations typically occur just above closed shells for particle numbers close to the so-called octupole magic numbers. Three of these, $N_{\text{oct}} = 56, 88, 134$, correspond well to three regions of octupole deformation in Fig. 8. We find no stable octupole deformed minima near the lightest traditional octupole magic number, $N_{\text{oct}} = 34$, likely because in such light nuclei octupole correlations are not strong enough to produce static octupole deformation in a mean-field calculation. Reflection asymmetry has a strong effect on the mass of exotic neutron-rich nuclei some of which gain almost 3 MeV of additional binding energy. The largest effect in our calculations is produced at $N = 190$, which is not typically cited as an octupole magic number but is where BSkG3 predicts that the intruder states emanating from the $k_{17/2}$ orbital mix with the many negative parity single-particle states just above $N = 184$. Our approach to obtaining the reflection asymmetric nuclei is based on the minimum energy of both configurations. Therefore there is no guarantee of any continuous behavior in β_{30} , only in energy. This can be noted in Fig. 8, where β_{30} increases at increasing N and abruptly goes to zero, which is not the case for the energy differences. This effect can be understood with the following: with increasing N , the octupole deformed minimum and the (typically prolate) reflection symmetric saddle point move away from each other in deformation space. When far enough from each other, their shell structure becomes sufficiently different such that both points on the PES do not depend in the same way on N . At some given neutron number, the reflection symmetric point achieves a lower value for the energy than the octupole one, resulting in a smooth change of energy difference, though not of octupole deformation.

The results shown in Fig. 8 are comparable to earlier global surveys of reflection asymmetry with EDF-based models, although these have all been limited to even-even nuclei while we include odd-mass and odd-odd isotopes. All models that we are aware of predict the two regions of octupole deformation within the experimentally accessible part of the nuclear chart, independently of whether they are based on a Skyrme-type, Gogny-type or relativistic EDF [53, 54, 136]. When calculations for exotic neutron-rich systems are available, all models generally also agree on the existence of the island of oc-

tupole deformation beyond $N \sim 184$ [53, 136]. The precise extent of the four regions in nucleon number varies strongly from one model to another, since whether or not octupole deformation appears in a given nucleus depends on single-particle properties as described above, but also on the models bulk properties such as its effective mass and its surface energy coefficient [135, 137, 138]. A few global studies of reflection asymmetry in the context of macroscopic-microscopic approaches are also available, but only find strong effects in the $Z \sim 88, N \sim 134$ region that are nevertheless smaller than those obtained in EDF-based models. Although not trivial, this last observation seems natural since we established that the effect of triaxiality turns out larger in self-consistent EDF-based models than in microscopic-macroscopic approaches [21, 83].

The impact of reflection asymmetry on the nuclear binding energy is not directly experimentally observable, and the presence of (static) octupole deformation is mostly inferred through other observables such as the appearance of rotational bands of alternating parity and enhanced $E1$ transitions, or even indirectly through the trends of charge radii [139] or the momentum distribution of particles emitted in heavy-ion collisions [140]. Most available experimental information concerns the $Z \sim 88, N \sim 134$ region and (to a lesser extent) the $Z \sim 56, N \sim 88$ region [56], in agreement with our calculations. Even though such studies on octupole deformation are even less numerous than those dealing with triaxiality, Coulomb excitation experiments such as those of Ref. [141, 142] directly confirm the presence of static octupole deformation in both regions.

We defer a more detailed study of reflection asymmetry to future work and limit ourselves for this study to the effect of reflection asymmetry on binding energies from an astrophysical point of view. We expect that the region of octupole deformation near $N \sim 190$ will be the most consequential since the effect on the binding energy is large and typical r-process trajectories produce a significant population of nuclei in this region before neutron irradiation ends. Our calculations point to two potentially significant effects: enhanced stability with respect of fission and the modification of the neutron dripline in this region. All else being equal, an additional contribution to the binding energy of 2 MeV of a nucleus effectively enlarges its fission barrier by the same amount and makes the spontaneous or induced fission of such a system dramatically less likely. This is likely to impact r-process simulations, since the fission properties of nuclei in this region determine for example the production of stable isotopes for $110 \leq A \leq 170$, but also impact the heating rate of kilonovae at late times through the (possible) produc-

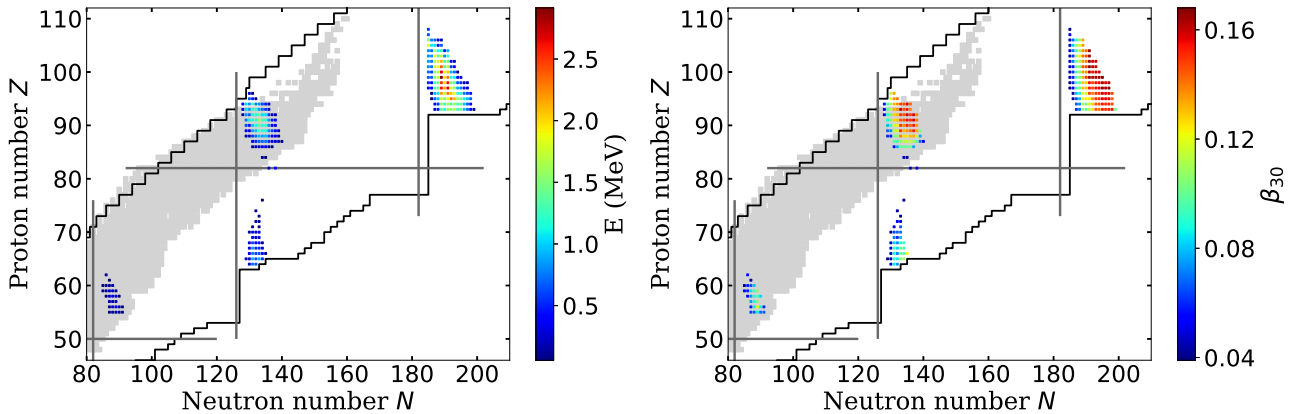


Fig. 8 Left: Binding energy differences between calculations restricted to quadrupole deformations and to calculations that allow for octupole shapes. Right: octupole deformation β_{30} . Gray shadow shows the experimental nuclei and black lines indicate BSkG3 drip lines.

tion of superheavy elements [143, 144]. The effect on the neutron dripline then simply enlarges the possibilities for the r-process to create exotic isotopes: for the Np($Z = 93$) and Pu($Z = 94$) isotopes, the additional binding energy due to reflection asymmetry extends the dripline from $N = 189$ to $N = 209$ and $N = 207$, respectively.¹³

To end this subsection, we remark again on the absence of any β_{32} deformation. Nuclei in our calculations are free to take non-axially symmetric shapes that are also asymmetric under reflection, and hence could a priori take advantage of this type of deformation to lower their total energy. Only a handful of nuclei exploit this possibility but the associated values of β_{32} are tiny: the largest value in absolute sense we obtain is -0.038 for ^{196}Eu . We take this as an indication that this type of deformation is not very relevant to nuclear ground states from a global point of view, although we mention that there are some indications that a very limited number of isotopes could exhibit non-axial octupole deformation in their ground state without any accompanying quadrupole deformation [145]. We refrain however from drawing too strong conclusions, since our numerical search for the nuclear ground state was not completely general and possibly biased by our inclusion of a temporary constraint on β_{30} in every calculation, as explained in Sec. 2.2.

4.6 Actinide fission barriers

To study the performance of the new model for static fission properties, we show in Fig. 9 the deviations of

¹³There is a similar but less dramatic effect for $Z = 64$ and 65 : reflection asymmetry is responsible for extending the neutron dripline by four neutrons.

BSkG2 and BSkG3 calculations with respect to the reference values: 45 primary barriers (top panel) and 45 secondary barriers (middle panel) of the RIPL-3 database [85] and 28 isomer excitation energies (bottom panel). As discussed in Sec. 4, BSkG3 offers significantly reduced mean deviations for all three fission properties compared to its predecessor, particularly for the isomer excitation energies. The new model also improves on the rms deviations for the primary barriers and isomer excitation energies resulting in a smaller spread of the values in the top and bottom panels of Fig. 9, at the cost of a slightly less accurate description of the secondary barriers in the middle panel.

The new model now describes all primary barriers for $Z \geq 90$ nuclei in RIPL-3 within 1 MeV. We repeat the observations of Ref. [42]: this performance with respect to the static fission properties is not universal among EDF-based models in the literature. When the physics of large deformation is not included in the parameter adjustment, the predictions of such a model can be off by up to 10 MeV [30]. We ascribe the success of both BSkG2 and BSkG3 to (i) the inclusion of fission properties in the parameter adjustment and (ii) our three-dimensional calculations of the fission PES that allow for nuclear shapes with triaxial and octupole deformation [83]. The BSkG2 and BSkG3 PESes for actinide nuclei and the fission paths obtained from them are qualitatively similar, we do not show any of them here but refer the interested reader to Ref. [83]. We only mention that, as for BSkG2, the fission paths of essentially all nuclei we consider exploit triaxial deformation to lower both barriers significantly, combining a finite value of the triaxiality angle γ with finite octupole deformation near the outer barrier.

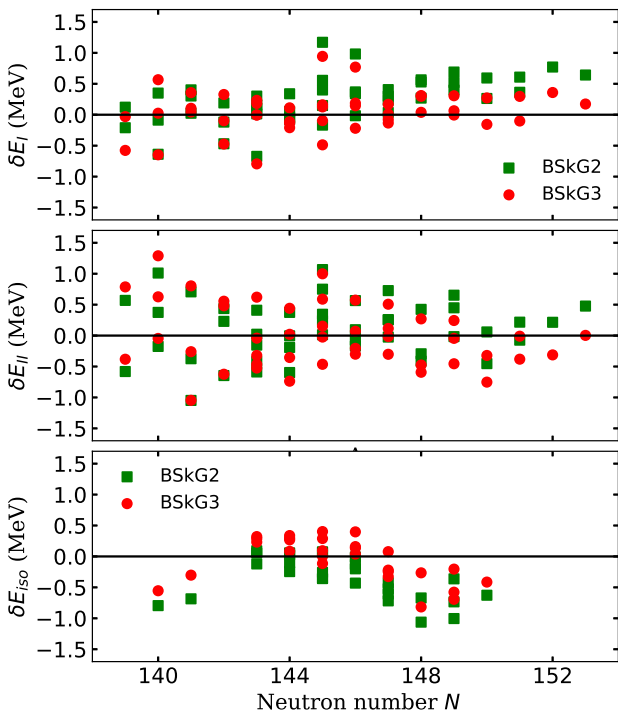


Fig. 9 Difference between calculated and reference values [85, 99] for the three different static fission properties (E_I , E_{II} and E_{iso}) as a function of neutron number for BSkG2 (green squares) and BSkG3 (red circles).

We did not start the development of BSkG3 with the aim to further improve its description of the physics at large deformations and thus did not anticipate its improved fission properties as compared to BSkG2. In an attempt to explain the differences, we investigated the surface energy and surface symmetry coefficients of both models through ETFSI calculations of semi-infinite nuclear matter along the lines of Ref. [30, 146]. Both models have an essentially identical surface energy coefficient $a_{\text{surf}}^{\text{ETF}} = 17.5 \text{ MeV}^{14}$ but have different surface symmetry coefficients $a_{\text{s,surf}}^{\text{ETF}}$: they amount to -60.5 and -51.3 MeV for BSkG2 and BSkG3, respectively. These values both fall within the (large) spread of predictions of other Skyrme-based models [147].

We show the difference between the primary fission barriers obtained with BSkG3 and BSkG2 in Fig. 10, both as a function of mass number A (top panel) and asymmetry $I = (N - Z)/(N + Z)$ (bottom panel). This

¹⁴This value differs from the value we quoted for BSkG2 in Ref. [83], $a_{\text{surf}}^{\text{HF}} = 17.9 \text{ MeV}$. In Ref. [83] however, we relied on Hartree-Fock calculations of semi-infinite nuclear matter. Different approaches provide absolute values for a_{surf} that can differ by up to 1 MeV, but the differences between parameterisations are robust across many-body methods, see the discussion in Ref. [30].

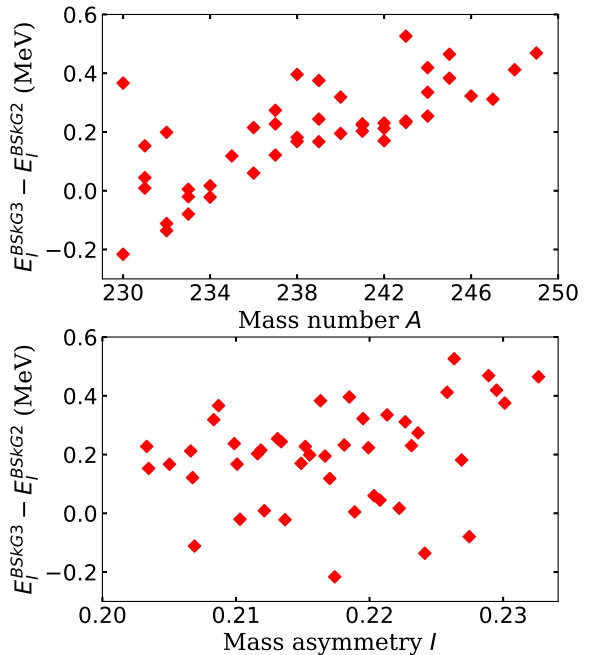


Fig. 10 Differences between calculated values for the primary fission barrier heights with BSkG3 and BSkG2 as a function of atomic mass A (upper panel) or mass asymmetry I (lower panel).

figure shows that the differences between both models are not large (less than 600 keV for any given nucleus) but that the predicted mass trends nevertheless differ. Despite what one would naively expect from the difference in $a_{\text{s,surf}}^{\text{ETF}}$, there is no clear trend with asymmetry to be discerned although this could simply be due to the limited variation of I spanned by the nuclei for which empirical barriers are available.

Since BSkG3 differs from BSkG2 in many respects, we are unable to pinpoint a single source of the improved performance of the former but conclude that the differences arise from a multitude of (possibly competing) effects. One is simply the inclusion of the entire set of 45 nuclei in the fitting protocol, as opposed to just the properties of twelve even-even nuclei as for BSkG2. The extended form of the EDF and the more microscopic treatment of pairing could also each contribute to the differences between both models, as could the vibrational correction which is significantly smaller in the new model. A detailed analysis including nuclei outside of the actinide region is needed to disentangle these effects but is beyond the scope of this work. For now, we only note that the different mass trend and $a_{\text{s,surf}}$ will likely result in varying predictions regarding the fission properties of extremely neutron-rich isotopes, even if they produce modest variations for the fission barriers of actinide nuclei.

5 Infinite nuclear matter properties

We present in Tab. 3 the properties of INM at saturation for BSk31 [23], BSkG2 [24] and BSkG3. We show, from top to bottom, the Fermi momentum k_F , the saturation density ρ_{sat} , the energy per particle of symmetric matter at saturation a_v , the symmetry energy coefficient J , the slope of the symmetry energy L , the isoscalar (isovector) effective mass M_s^*/M (M_v^*/M), the compressibility modulus K_v , the isovector component of the compressibility coefficient K_{sym} , the skewness parameter K' and the Landau parameters G_0 and G'_0 of symmetric INM. Note that BSkG2 constrained the value of $J = 32$ MeV to obtain a minimum stiffness of the symmetry energy of the model. For BSkG3, we fix $J = 31$ MeV, as previously done for BSk31, since we can achieve a stiff symmetry energy thanks to the extended Skyrme form and the new constraint at high density. Among all parameters of Tab. 3, we note a major difference on K_{sym} ; BSkG2 presents a much lower value compared to BSkG3 and BSk31. This nuclear parameter still presents a large uncertainty. Different estimations, from unitary-gas considerations [148], neutron skin of ^{48}Ca and ^{208}Pb [149], and theoretical predictions based on the equilibrium density of nuclear matter lead to negative values ≈ -100 MeV (± 100 MeV) [150]. Therefore, all three values are within the current uncertainty range. This parameter is obtained through the second derivative of the symmetry energy with respect to the density and evaluated at saturation. Since it is a high-order parameter of nuclear matter, K_{sym} is a measure of the stiffness of the symmetry energy at intermediate-high densities of a given model. The parameterisations BSk31 and BSkG3 were constrained to reproduce stiff NeutM EoS at high densities, as required by the existence of pulsars with $M > 2M_\odot$. It is, therefore, natural that these models yield higher (less negative) values for K_{sym} than BSkG2.

It is interesting to note the differences in the INM parameters when constructing a model that reconciles an excellent reproduction of nuclear data with NS properties. Values of the low-order nuclear parameters, as the first four lines of Tab. 3, are essential to the success of the mass table. In turn, the high-order ones, as K_{sym} , play no role in the nuclear masses but strongly impact the high-density EoS and NS properties. Note also that the impact of K_{sym} value is model dependent. A $K_{\text{sym}} < -100$ MeV (as obtained in BSkG2) does not necessarily lead to incompatibility with NS data for all possible models. A recent study [151] presents a set of EoS with K_{sym} ranging from $+20$ MeV to -208 MeV, which successfully reproduces the properties of NS.

Table 3 INM properties for the BSk31 [23], BSkG2 [24] and BSkG3 parameterisations. See Refs. [23, 152, 153] for the various definitions.

Properties	BSk31	BSkG2	BSkG3
k_F [fm]	1.3290	1.3265	1.3270
ρ_{sat} [fm^{-3}]	0.15855	0.15767	0.15784
a_v [MeV]	-16.110	-16.070	-16.082
J [MeV]	31.000	32.000	31.000
L [MeV]	53.076	53.027	55.061
M_s^*/M	0.84000	0.86000	0.85860
M_v^*/M	0.73246	0.77330	0.72171
K_v [MeV]	244.01	237.45	242.56
K_{sym} [MeV]	-15.780	-150.60	-21.248
K' [MeV]	302.97	376.26	304.17
G_0	0.36551	0.35846	0.20046
G'_0	0.96946	0.97873	0.97812

We show in the bottom panels of Fig. 11 the NeutM energy for BSkG3, BSkG2 and BSk31 and compare with the ab-initio calculations of WFF [156], APR [157], LS2 [158] and FP [159]. Chiral interactions predictions are represented by LTC [160] and DHC [15] bands. At densities close to saturation and below (bottom left) all models present similar behavior, and are in good agreement with the ab-initio calculations. At high densities, however, the BSkG3 and BSk31 parameterisations present a much stiffer behaviour when compared to BSkG2 and are in good agreement with the LS2 EoS [158]. This figure highlights the main improvement in the BSkG3 INM properties compared to our previous BSkG1 and BSkG2, which is the stiffness of the NeutM energy at high densities. The typical central density in NSs cores computed with Skyrme EDFs reaches 6-10 times saturation density depending on the stiffness of the EoS. However, EDFs fitted to experimental atomic masses only, remain poorly constrained at densities well above saturation density. The EoSs obtained with standard Skyrme EDFs are generally found to be too soft at high densities to explain the existence of the most massive observed NS. As shown, e.g., in Ref [161], the EoS can be made stiff enough by introducing t_4 and t_5 terms without deteriorating the quality of the fit to atomic masses. Top panels of Fig. 11 display the symmetry energy for BSkG3, BSkG2, and BSk31. Note that we use the definition of symmetry energy as the energy necessary to convert symmetric nuclear matter (SNM) into pure NeutM: $e_{\text{sym}} = e_{\text{NeutM}} - e_{\text{SNM}}$. The top left panel compares the model predictions for e_{sym} with experiments constraints from the isobaric analog state (IAS) and IAS + neutron skin, Δr_{np} (blue and dark blue), from Ref. [154] The yellow band shows the PREX-II predictions for the symmetry energy, where we vary $J = 38.1 \pm 4.7$ MeV and $L = 106 \pm 37$ MeV as suggested by Ref. [155]. Note that all models repro-

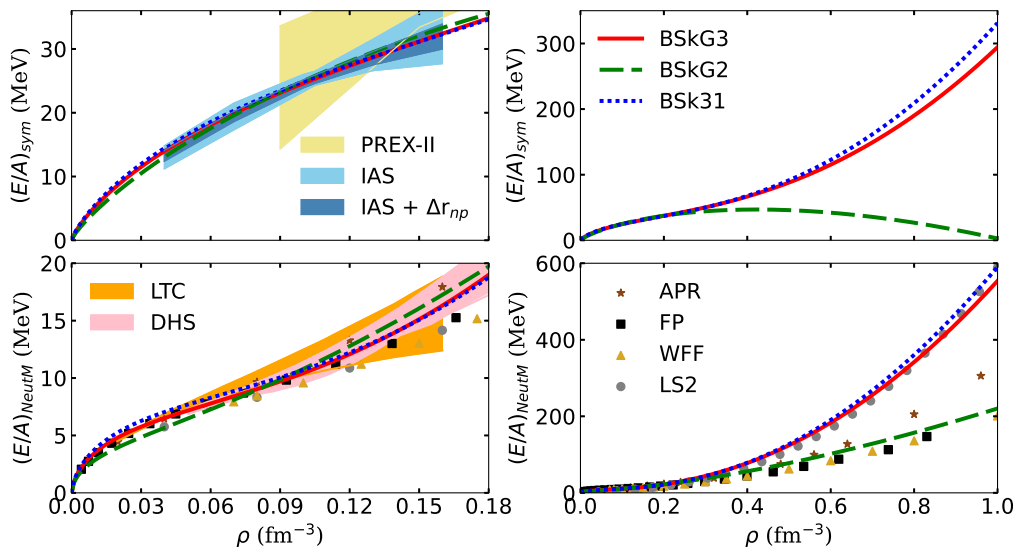


Fig. 11 Top (bottom) panels show the symmetry (neutron matter) energy per nucleon as a function of the baryon density for BSkG3 (continuous red), BSkG2 (dashed green), and BSk31 (dotted blue). Left panels show the predictions at densities below and around saturation while the right panels display the results at high densities. The models predictions are compared with experimental constraints [154, 155] and ab-initio calculations of WFF [156], APR [157], LS2 [158], FP [159], LTC [160] and DHC [15].

duce well the experimental constraints given by the blue bands (IAS and IAS + Δr_{np}). However, models underestimate PREX-II at saturation and higher densities, being inside the yellow band just at low densities. This demonstrates again the tension raised by PREX-II results when compared with other experiments and theory predictions, as mentioned in Sec. 4.1. The top right panel of Fig. 11 shows the symmetry energy at high densities, where the effect of the stiff NeutM EoS can be observed avoiding the collapse of e_{sym} for BSkG3 and BSk31, in contrast to BSkG2.

The density dependence of the effective mass is shown in Fig. 12 for BSkG3 and compared with BSkG2 and BSk31. We note that for the isoscalar channel, the effective mass obtained with BSkG3 is almost identical to that of BSk31; it is close to that of BSkG2 up to $\rho \approx 0.2 \text{ fm}^{-3}$ but is significantly smaller at higher densities. Note that BSkG2, BSkG3 and BSk31 are in close agreement with the extended Brueckner-Hartree-Fock (EBHF) calculations of Ref. [101], as shown in the insert plot in the top panel. For the isovector effective mass, BSkG3 is similar to BSk31, and lower than BSkG2, at lower densities. From densities around 0.3 fm^{-3} and beyond its value lies in between BSkG2 and BSk31 predictions. Moreover, BSkG3 shows $M_s^*/M = 0.859$ at saturation which is in good agreement with values obtained by EBHF calculations [101, 162]. Table 3 shows that BSkG3 values for M_s^*/M and M_v^*/M taken at saturation present the hierarchy $M_s^* > M_v^*$, which implies

that the neutron effective mass is higher than the proton one in neutron-rich matter. This hierarchy between neutron and proton effective mass is consistent with measurements of the isovector giant dipole resonance [163] and ab-initio calculations [50, 101]. In particular, the BSkG3 magnitude of the splitting at saturation density is in excellent agreement with the realistic calculation of Ref. [101].

We show in Fig. 13 the distribution of the potential energy among the four two-body spin-isospin (S, T) channels for BSkG3 (continuous red), BSkG2 (dashed green) and BSk31 (dotted blue). We compare our results with two different Brueckner-Hartree-Fock (BHF) calculations labeled "Catania 1" [164] and "Catania 2" [165]. The model predictions for BSkG3 can be considered as satisfactory given the current uncertainty on what the real distribution actually is.

To summarize this section, we emphasise that BSkG3 exhibits INM properties at saturation that are similar to those of the previous BSkG models [21, 24] (see Tab. 3) with two important improvements: we now produce a stiff NeutM EoS at high densities (Fig. 11) which is important for explaining NSs with more than $2M_\odot$, and replace the phenomenological pairing interaction of previous models by a more microscopically grounded interaction designed to match the 1S_0 pairing gaps in INM deduced from ab initio calculations (Fig. 1).

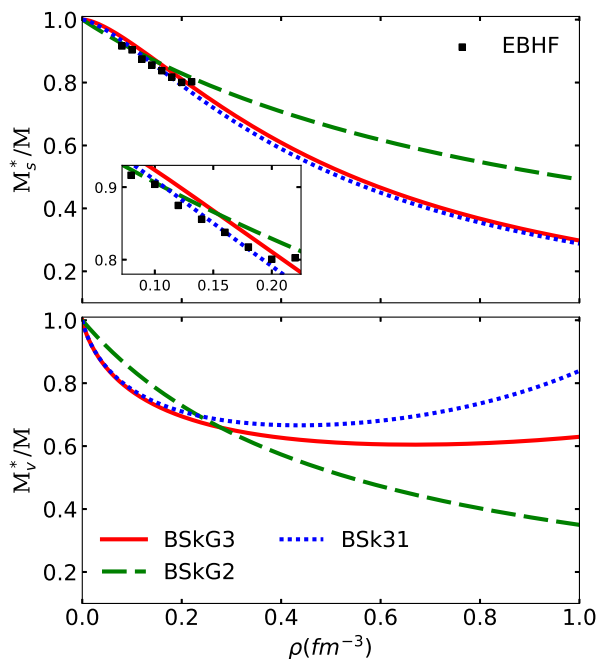


Fig. 12 Isoscalar (top) and isovector (bottom) effective mass as a function of the baryon density for BSkG3 (continuous red), BSkG2 (dashed green), and BSk31 (dotted blue). In the upper panel we compare the isoscalar effective mass with the EBHF calculations from Ref. [101].

6 Neutron star properties

In this section, the NS properties obtained with the new BSkG3 parameterisation are explored. We show in Fig. 14 the NS mass and radius relations for BSkG2, BSkG3, and BSk31. We compare the model predictions with the observational data from X-ray emissions of NICER [46, 166, 167] and the GW170817 observation from the LIGO/Virgo interferometers [168]. The tidal deformability is strongly correlated to the NS mass and radius (see, e.g., Ref. [169] and references therein), converting the uncertainty on $\tilde{\lambda}$ into an uncertainty on the radius of a $1.4M_{\odot}$ NS, as shown in the light gray contour in Fig. 14 indicated by “GW170817”.

We note that BSkG3 and BSk31 models are compatible with all observational data while BSkG2 fails to reach the required maximum mass of $2M_{\odot}$. This is a direct effect of the stiffness of the NeutM EoS, since the β -equilibrated matter contained in NSs is extremely neutron-rich. To obtain the NS macroscopic properties of Fig. 14, we estimate the NSs masses and radii as follows. First, we integrate the Tolman-Oppenheimer-Volkoff equations [170, 171] from the center of the star up to the crust-core transition fixed at the baryon number density $n_{cc} = 0.08 \text{ fm}^{-3}$. The core is described using the corresponding EoS of neutron-proton-electron-

Table 4 NS properties obtained with BSk31, BSkG2 and BSkG3 parameterizations. We show in the first row the radius of the canonical NS of $1.4M_{\odot}$; the following three lines give the mass, radius and energy density for the most compact NS. $\mathcal{E}_{\text{causal}}$ denotes the energy density for which causality is violated. Next we show the threshold energy density and NS mass for the onset of the dUrca process and the energy density $\mathcal{E}_{\text{pQCD}}$ up to which the model is consistent with constraints derived from pQCD (see text for details).

Properties	BSk31	BSkG2	BSkG3
$R_{1.4}$ [km]	12.71	11.53	12.73
M_{max} [M_{\odot}]	2.26	1.82	2.26
$R_{M_{\text{max}}}$ [km]	11.11	9.66	11.10
$\mathcal{E}_{M_{\text{max}}}$ [$10^{15} \text{ g cm}^{-3}$]	2.276	3.192	2.273
$\mathcal{E}_{\text{causal}}$ [$10^{15} \text{ g cm}^{-3}$]	2.392	6.558	2.381
$\mathcal{E}_{\text{dUrca}}$ [$10^{14} \text{ g cm}^{-3}$]	7.166	–	7.136
M_{dUrca} [M_{\odot}]	1.40	–	1.38
$\mathcal{E}_{\text{pQCD}}$ [$10^{15} \text{ g cm}^{-3}$]	2.509	4.289	2.508

muon ($npe\mu$) matter in β equilibrium as in Ref. [172]. In this way, we obtain the mass M_{core} and radius R_{core} of the NS core. From the approximate formulas given in Ref. [173], we infer the NS mass and radius:

$$M = M_{\text{core}} + M_{\text{crust}}, \quad (23)$$

$$R = R_{\text{core}} \left\{ 1 - \left[\left(\frac{\mu_{\text{cc}}}{\mu_0} \right)^2 - 1 \right] \left(\frac{R_{\text{core}} c^2}{2GM} - 1 \right) \right\}^{-1}, \quad (24)$$

with

$$M_{\text{crust}} = 7.62 \times 10^{-2} M_{\odot} \left(\frac{P_{\text{cc}}}{\text{MeV fm}^{-3}} \right) \times \left(1 - \frac{2GM_{\text{core}}}{R_{\text{core}} c^2} \right) \left(\frac{R_{\text{core}}}{10 \text{ km}} \right)^4 \left(\frac{M_{\odot}}{M_{\text{core}}} \right). \quad (25)$$

Here μ_{cc} and μ_0 denote the baryon chemical potentials at the crust-core transition and at the stellar surface, respectively. For cold catalyzed matter, the latter coincides with the mass per nucleon of ^{56}Fe . P_{cc} represents the pressure at the crust-core transition.

In Table 4, we indicate the NS properties for BSk31, BSkG2, and BSkG3. The first three rows correspond, respectively, to the radius of the canonical $1.4 M_{\odot}$ NS, the maximum mass of NS and its respective radius. We have also computed the energy density $\mathcal{E}_{\text{causal}}$ of beta-equilibrated matter for which the sound speed becomes higher than the speed of light. We remark that $\mathcal{E}_{\text{causal}}$ for BSkG3 is higher than the energy density $\mathcal{E}_{M_{\text{max}}}$ at the center of the most massive NS, as seen in Table 4. Therefore none of the models presented here violates causality.

Table 4 also shows the density and the corresponding NS mass for which the proton fraction inside the

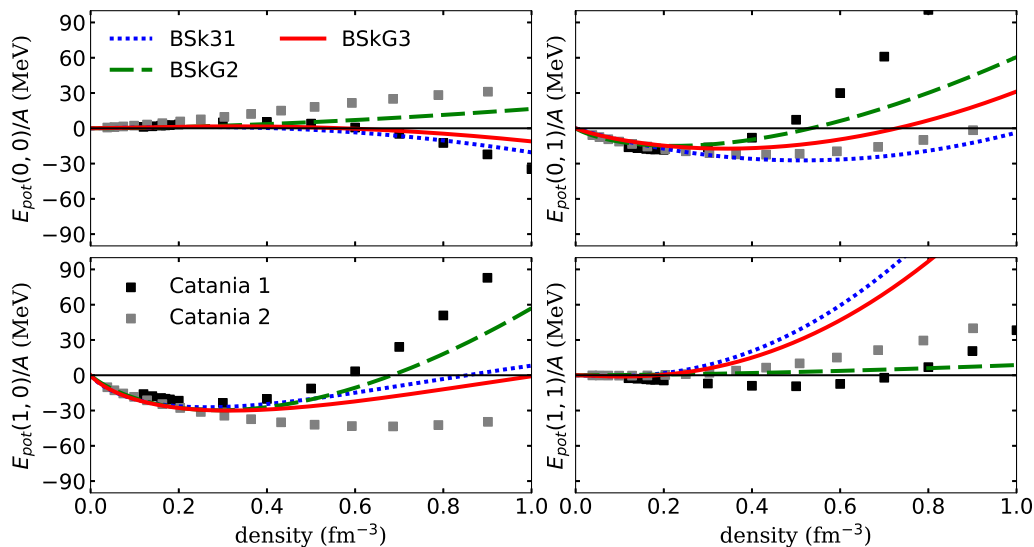


Fig. 13 Potential energy per particle in each (S,T) channel as a function of the baryon density for charge-symmetric nuclear matter for BSk31 (dotted blue), BSkG2 (dashed green) and BSkG3 (continuous red). Black and gray squares correspond to the "Catania 1" [164] and "Catania 2" [165] BHF calculations, respectively.

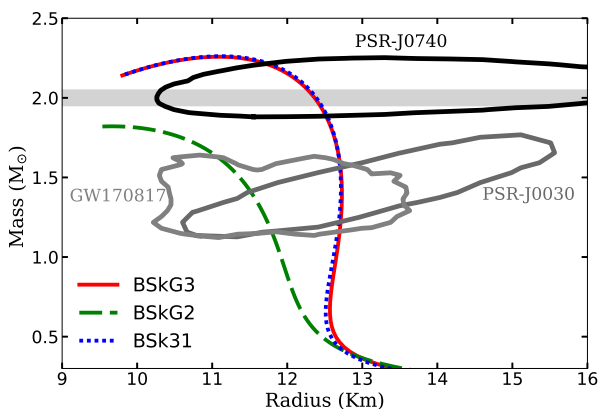


Fig. 14 Mass – radius relation for BSkG3 (solid red line), BSkG2 (dashed green line) and BSk31 (dotted blue line). Contours show the NICER observations for the pulsars PSR-J0030 [166] and PSR-J0740 [46, 167] together with LIGO/Virgo observation of GW170817 [168]. The gray band indicates the maximum mass constraint of $2M_{\odot}$ NS [44, 174]. See text for more details.

star reaches the threshold for the onset of the direct Urca (dUrca) process [175] for the three models. This process is required to interpret the observed thermal luminosity of some NSs [176]. The model BSkG2 does not fulfill this constraint. BSk31 and BSkG3 models allow for the dUrca process for NSs with a mass above $\sim 1.4 M_{\odot}$.

Our models can be further tested using results from perturbative quantum chromodynamics (pQCD) calculations: assuming only causality and thermodynamic consistency, pQCD predictions at extreme densities ($\gtrsim 40 \rho_{\text{sat}}$)

impose constraints on the EoS at lower densities [177]. We have verified that the BSkG3 EoS is consistent with this constraint up to an energy density $\epsilon_{\text{pQCD}} = 2.508 \times 10^{15}$ [g cm³], i.e. above the density of the most massive NS predicted by this model. BSk31 and BSkG2 also satisfy this constraint.

7 Conclusions and outlook

We have presented a new entry in the BSkG-series of EDF-based models. BSkG3 takes up the challenge of describing dense matter in a vast range of density regimes, combining a sophisticated description of thousands of atomic nuclei at saturation density in terms of symmetry-broken mean-field configurations with realistic predictions for dense matter at higher densities, such as encountered in NSs. The key to achieving both goals is the form of the functional: we move here to the extended form of Ref. [52] that includes additional density dependencies compared to the traditional Skyrme form.

In contrast to its predecessors, the new model predicts an EoS of dense matter that is entirely compatible with the most recent theoretical and observational NS constraints, including the existence of heavy pulsars with $M \geq 2M_{\odot}$. We have also refined our approach to nucleon pairing, rendering the model more suited to the treatment of superfluidity in different NS layers by replacing the standard (and entirely phenomenological) ansatz for the pairing EDF with a more microscopically founded prescription designed to match the 1S_0

pairing gaps in INM as obtained from realistic EBHF calculations.

BSkG3 also describes nuclear properties with increased accuracy compared to BSkG2: we report rms deviations of 0.631 MeV on 2457 atomic masses and 0.0237 fm for 810 charge radii. These global deviations remain larger than the lowest ever achieved by the BSk models, but BSkG3 essentially matches the performance of the best of the older models for mass differences. In addition to this quantitative improvement, we have for the first time accounted for reflection asymmetry in the nuclear ground state in even-even, odd-mass and odd-odd nuclei alike. This further enriches the BSkG models in terms of collective effects and allows us to connect to the phenomenology of octupole deformation. Although the impact of this degree of freedom on the global accuracy of our model is small due to the limited number of nuclei impacted, we anticipate meaningful effects for nucleosynthesis simulations chiefly because of the large impact of octupole deformation on the ground states of exotic neutron-rich nuclei near $N \sim 190$. The accuracy of the new model extends beyond ground states to fission properties: BSkG3 reproduces the 45 RIPL-3 reference values for the primary barriers of actinide nuclei with a rms deviation of 0.33 MeV, combined with rms deviations on secondary barriers and isomeric excitation energies of 0.51 MeV and 0.34 MeV respectively. These values are, to the best of our knowledge, unmatched in the available literature.

This work addresses the extrapolation of the BSkG to high nucleon densities, but this is hardly the only extrapolation relevant to NS physics: a general-purpose EoS should not be limited to zero temperature but cover a range of temperatures, since the temperatures involved in core-collapse supernovae and NS mergers simulations can reach above 100 MeV [7, 178]. To enlarge the reach of the BSkG models, we plan to extend our fitting protocol to also include constraints on the properties of the EoS at finite temperature, as predicted by advanced many-body approaches such as for example Refs. [179–182].

We have several prospects to further improve our description of atomic nuclei. The accuracy we achieve here for fission barriers in the actinide region motivates us to extend our fission calculations to exotic neutron-rich nuclei. Although this is a monumental task because of the number of nuclei involved, efforts in this direction are under way. We also anticipate studying the issues touched upon in Sec. 2.3: like all EDF-based models, the BSkG-series do not describe a small but systematic contribution to the binding energy of odd-odd nuclei, contaminating all mass differences that involve such isotopes [97]. As suggested in Ref. [24], tuning the

proton-neutron spin-spin term in the time-odd part of the functional might provide a way forward. Our most ambitious and undoubtedly long-range goal is to improve our description of nuclear collective motion, abandoning simple recipes such as the rotational correction in favor for a more microscopic approach founded in beyond-mean-field techniques.

Acknowledgements We gratefully acknowledge useful discussions with both Dr. M. Bender and N. Shchepochin on the subject of surface tension and its isospin dependency. This work was supported by the Fonds de la Recherche Scientifique (F.R.S.-FNRS) and the Fonds Wetenschappelijk Onderzoek - Vlaanderen (FWO) under the EOS Projects nr O022818F and O000422F. The present research benefited from computational resources made available on the Tier-1 supercomputers Zenobe and Lucia of the Fédération Wallonie-Bruxelles, infrastructure funded by the Walloon Region under the grant agreement nr 1117545. Further computational resources have been provided by the clusters Consortium des Équipements de Calcul Intensif (CÉCI), funded by F.R.S.-FNRS under Grant No. 2.5020.11 and by the Walloon Region. G.S. is supported by U.S. Department of Energy, Office of Science, Grant No. DE-AC05-00OR22725. W.R. and S.G. gratefully acknowledge support by the F.R.S.-FNRS.

Appendix A: List of abbreviations

Abbreviation	Meaning
BSkG	Brussels-Skyrme-on-a-Grid
dUrca	direct Urca (process)
EDF	Energy density functional
EoS	Equation of state
INM	Infinite (homogeneous) nuclear matter
MLNN	Multilayer neural network
MOI	Moment of inertia
NeutM	Pure (infinite) neutron matter
$npe\mu$	neutron-proton-electron-muon
NS	Neutron star
SNM	symmetric (infinite) nuclear matter
PES	Potential energy surface
pQCD	Perturbative quantum chromodynamics
rms	root-mean-square
r-process	rapid neutron-capture process

Appendix B: Coupling constants of E_{Sk}

We include here the complete expressions for all coupling constants of the Skyrme energy densities in terms of the model parameters. The coupling constants ap-

pearing in the time-even, central part of the EDF are:

$$C_t^{\rho\rho}(\rho_0) = +C_{0t}^+(t_0, x_0) + \frac{1}{6}C_{0t}^+(t_3, x_3)\rho_0^\alpha, \quad (\text{B.1})$$

$$C_t^{\rho\tau}(\rho_0) = +\frac{1}{2}C_{0t}^+(t_1, x_1) + \frac{1}{2}C_{0t}^-(t_2, x_2) \\ + \frac{1}{2}C_{0t}^+(t_4, x_4)\rho_0^\beta + \frac{1}{2}C_{0t}^-(t_5, x_5)\rho_0^\gamma, \quad (\text{B.2})$$

$$C_t^{\rho\Delta\rho} = -\frac{3}{8}C_{0t}^+(t_1, x_1) + \frac{1}{8}C_{0t}^-(t_2, x_2), \quad (\text{B.3})$$

$$C_t^{\nabla\rho\nabla\rho}(\rho_0) = +\frac{3}{8}C_{0t}^+(t_4, x_4)\rho_0^\beta - \frac{1}{8}C_{0t}^-(t_5, x_5)\rho_0^\gamma, \quad (\text{B.4})$$

$$C_t^{\rho\nabla\rho\nabla\rho}(\rho_0) = -\frac{1}{2}C_{0t}^+(t_4, x_4)\rho_0^{\beta-1}, \quad (\text{B.5})$$

while those in the time-odd, central part $\mathcal{E}_{t,e}(\mathbf{r})$ are

$$C_t^{ss}(\rho_0) = C_{t,11}^+(t_0, x_0) + \frac{1}{6}C_{1t}^+(t_3, x_3)\rho_0^\alpha, \quad (\text{B.6})$$

$$C_t^{jj}(\rho_0) = -C_t^{\rho\tau}(\rho_0). \quad (\text{B.7})$$

We again draw the readers attention to a change of notation with respect to the BSkG1 and BSkG2 models: the exponent of the density in the expression for $C_t^{\rho\rho}(\rho_0)$ was denoted by γ in Refs. [21, 24], whereas here we indicate the same quantity here with α following Ref. [104].

We define the shorthands $C_{ST}^{+/-}(t, x)$ as in Ref. [61]:

$$C_{00}^+(t, x) = +\frac{3}{8}t, \quad C_{01}^+(t, x) = -\frac{1}{8}t - \frac{1}{4}tx, \\ C_{10}^+(t, x) = -\frac{1}{8}t + \frac{1}{4}tx, \quad C_{11}^+(t, x) = -\frac{1}{8}t, \\ C_{00}^-(t, x) = +\frac{5}{8}t + \frac{1}{2}tx, \quad C_{01}^-(t, x) = +\frac{1}{8}t + \frac{1}{4}tx, \\ C_{10}^-(t, x) = +\frac{1}{8}t + \frac{1}{4}tx, \quad C_{11}^-(t, x) = +\frac{1}{8}t. \quad (\text{B.8})$$

Finally, the coupling constants of the time-even spin-orbit part of the EDF are given in terms of the parameters W_0 and W'_0

$$C_0^{\rho\nabla\cdot J} = -\frac{W_0}{2} - \frac{W'_0}{4}, \quad C_1^{\rho\nabla\cdot J} = -\frac{W'_0}{4}. \quad (\text{B.9})$$

The time-odd spin-orbit coupling constants are identical to the time-even ones, i.e. $C_t^{j\nabla s} = C_t^{\rho\nabla\cdot J}$.

Appendix C: Rotational, vibrational and Wigner energies

For completeness, we briefly recall here the expressions for the rotational, vibrational, and Wigner energies as employed in the BSkG1, BSkG2 and BSkG3 models.

– *The rotational correction*

The rotational correction is based on a simple perturbative cranking model, involving the Belyaev moments of inertia (MOI) around the three principal axes of the nucleus, $\mathcal{I}_\mu^B(\mu = x, y, z)$ [183]:

$$E_{\text{rot}} = -\sum_{\mu=x,y,z} f_\mu^{\text{rot}} \frac{\langle \hat{J}_\mu^2 \rangle}{2\mathcal{I}_\mu^B}, \quad (\text{C.10a})$$

$$f_\mu^{\text{rot}} = b \tanh\left(c \frac{\mathcal{I}_\mu^B}{\mathcal{I}_c}\right), \quad (\text{C.10b})$$

where \hat{J}_μ is an angular momentum operator and $\mathcal{I}_C = \frac{2}{15}mR^2A$ is (one-third of) the MOI of a rigid rotor of radius $R = 1.2A^{1/3}$, comprised of A nucleons of average mass m . Both b and c are adjustable parameters, while the three MOI in Eq. (C.10a) are calculated consistently from the HFB auxiliary state.

– *The vibrational correction*

The vibrational correction is given by:

$$E_{\text{vib}} = -\sum_{\mu=x,y,z} f_\mu^{\text{vib}} \frac{\langle \hat{J}_\mu^2 \rangle}{2\mathcal{I}_\mu^B}, \quad (\text{C.11a})$$

$$f_\mu^{\text{vib}} = dB_\mu e^{-l(B_\mu - B_0)^2}, \quad (\text{C.11b})$$

$$B_\mu = \frac{\mathcal{I}_\mu^B}{\mathcal{I}_c}. \quad (\text{C.11c})$$

where d, l and B_0 are model parameters. Note that Eq. (C.11a) only intends to capture the deformation dependence of the vibrational energy, as discussed in Ref. [24, 98].

– *The Wigner energy*

Mean-field models that describe the nucleus with separate proton and neutron treatments typically underestimate the binding energy of $N \simeq Z$ nuclei. To rectify this issue, the BSkG models include the Wigner energy correction of Ref. [184]:

$$E_W = V_W \exp(-\lambda((N - Z)/A)^2) \\ + V'_W |N - Z| \exp[-(A/A_0)^2], \quad (\text{C.12})$$

with four adjustable parameters V_W, V'_W, λ , and A_0 .

Appendix D: Explanation of the supplementary material

We provide as supplementary material the files `Mass_Table_BSkG3.dat` and `Fission_Table_BSkG3.dat`. The former contains the calculated ground state properties of all nuclei with $8 \leq Z \leq 118$ lying between the proton and neutron drip lines. The latter contains the fission barriers and isomer excitation energies as

calculated for all 45 nuclei with $Z \geq 90$ that figure in the RIPL-3 database. The contents of both files follow the conventions of the supplementary files of Refs. [21, 24] and [83] with only two exceptions. First, we now also list the octupole deformations β_{30} and β_{32} among ground state properties. Second, for odd-mass and odd-odd nuclei with finite octupole deformation we can no longer assign a parity quantum number to the calculated ground states; in such cases we set the final two columns of `Mass_Table_BSKG3.dat` that contain the parities of the blocked quasiparticle(s) to zero. For convenience, we repeat the contents of all columns of both files in Tables 5 and 6.

References

1. Y.T. Oganessian, V.K. Utyonkov, Y.V. Lobanov, F.S. Abdullin, A.N. Polyakov, R.N. Sagaidak, I.V. Shirokovsky, Y.S. Tsyganov, A.A. Voinov, G.G. Gulbekian, S.L. Bogomolov, B.N. Gikal, A.N. Mezentssev, S. Iliev, V.G. Subbotin, A.M. Sukhov, K. Subotic, V.I. Zagrebaev, G.K. Vostokin, M.G. Itkis, K.J. Moody, J.B. Patin, D.A. Shaughnessy, M.A. Stoyer, N.J. Stoyer, P.A. Wilk, J.M. Kenneally, J.H. Landrum, J.F. Wild, R.W. Loughheed, *Phys. Rev. C* **74**(4), 044602 (2006). DOI 10.1103/PhysRevC.74.044602. Publisher: American Physical Society
2. A.S. Eddington, *Nature* **106**(2653), 14 (1920). DOI 10.1038/106014a0. URL <https://www.nature.com/articles/106014a0>
3. D. Blaschke, N. Chamel, in *Astrophysics and Space Science Library*, vol. 457, ed. by L. Rezzolla, P. Pizzonechero, D.I. Jones, N. Rea, I. Vidaña (2018), vol. 457, p. 337. DOI 10.1007/978-3-319-97616-7_7
4. N. Chamel, P. Haensel, *Living Rev. Relativ.* **11**, 10 (2008)
5. D.G. Ravenhall, C.J. Pethick, J.R. Wilson, *Phys. Rev. Lett.* **50**(26), 2066 (1983). DOI 10.1103/PhysRevLett.50.2066. URL <https://link.aps.org/doi/10.1103/PhysRevLett.50.2066>. Publisher: American Physical Society
6. M.a. Hashimoto, H. Seki, M. Yamada, *Progress of Theoretical Physics* **71**(2), 320 (1984). DOI 10.1143/PTP.71.320. URL <https://doi.org/10.1143/PTP.71.320>
7. M. Oertel, M. Hempel, T. Klähn, S. Typel, *Rev. Mod. Phys.* **89**(1), 015007 (2017). DOI 10.1103/RevModPhys.89.015007. URL <https://link.aps.org/doi/10.1103/RevModPhys.89.015007>. Publisher: American Physical Society
8. P. Danielewicz, R. Lacey, W.G. Lynch, *Science* **298**(5598), 1592 (2002). DOI 10.1126/science.1078070. URL <https://www.science.org/doi/10.1126/science.1078070>. Publisher: American Association for the Advancement of Science
9. A. Sorensen, K. Agarwal, K.W. Brown, Z. Chajecki, P. Danielewicz, C. Drischler, S. Gandolfi, J.W. Holt, M. Kaminski, C.M. Ko, R. Kumar, B.A. Li, W.G. Lynch, A.B. McIntosh, W. Newton, S. Pratt, O. Savchuk, M. Stefaniak, I. Tews, M.B. Tsang, R. Vogt, H. Wolter, H. Zbroszczyk, A. Andronic, S.A. Bass, A. Chbihi, M. Colonna, M.D. Cozma, V. Dexheimer, X. Dong, T. Dore, L. Du, S.P. Harris, H.Z. Huang, J.C. Jiménez, J. Kapusta, A.L. Fèvre, L. McLerran, J. Noronha-Hostler, C. Plumberg, J. Randrup, S. Reddy, H.R. Schmidt, P. Senger, R. Seto, C. Shen, J. Steinheimer, J. Stroth, C. Sturm, K.J. Sun, W. Trautmann, G. Verde, V. Vovchenko, N. Xu. *Dense Nuclear Matter Equation of State from Heavy-Ion Collisions* (2023). DOI 10.48550/arXiv.2301.13253. URL <http://arxiv.org/abs/2301.13253>. ArXiv:2301.13253 [nucl-ex, physics:nucl-th]
10. M. Arnould, S. Goriely, *Progress in Particle and Nuclear Physics* **112**, 103766 (2020)
11. B.D. Metzger, G. Martínez-Pinedo, S. Darbha, E. Quataert, A. Arcones, D. Kasen, R. Thomas, P. Nugent, I.V. Panov, N.T. Zinner, *Monthly Notices of the Royal Astronomical Society* **406**(4), 2650 (2010). DOI 10.1111/j.1365-2966.2010.16864.x. URL <https://academic.oup.com/mnras/article-lookup/doi/10.1111/j.1365-2966.2010.16864.x>
12. D. Kasen, B. Metzger, J. Barnes, E. Quataert, E. Ramirez-Ruiz, *Nature* **551**(7678), 80 (2017). DOI 10.1038/nature24453
13. H. Hergert, *Front. Phys.* **8**, 379 (2020). DOI 10.3389/fphy.2020.00379. URL <https://www.frontiersin.org/article/10.3389/fphy.2020.00379/full>
14. B. Hu, W. Jiang, T.e.a. Miyagi, *Nat. Phys.* **18**, 1196 (2022)
15. C. Drischler, K. Hebeler, A. Schwenk, *Phys. Rev. Lett.* **122**, 042501 (2019)
16. M. Bender, P.H. Heenen, P.G. Reinhard, *Rev. Mod. Phys.* **75**(1), 121 (2003). DOI 10.1103/RevModPhys.75.121. URL <https://link.aps.org/doi/10.1103/RevModPhys.75.121>
17. J.W. Negele, D. Vautherin, *Phys. Rev. C* **5**(5), 1472 (1972). DOI 10.1103/PhysRevC.5.1472. URL <https://link.aps.org/doi/10.1103/PhysRevC.5.1472>
18. B.G. Carlsson, J. Dobaczewski, *Phys. Rev. Lett.* **105**(12), 122501 (2010). DOI 10.1103/PhysRevLett.105.122501. URL <https://link.aps.org/doi/10.1103/PhysRevLett.105.122501>
19. M. Stoitsov, M. Kortelainen, S.K. Bogner, T. Duguet, R.J. Furnstahl, B. Gebremariam, N. Schunck, *Phys. Rev. C* **82**(5), 054307 (2010). DOI 10.1103/PhysRevC.82.054307. URL <https://link.aps.org/doi/10.1103/PhysRevC.82.054307>
20. R.N. Perez, N. Schunck, A. Dyhdalo, R.J. Furnstahl, S.K. Bogner, *Phys. Rev. C* **97**(5), 054304 (2018). DOI 10.1103/PhysRevC.97.054304. URL <http://arxiv.org/abs/1801.08615>. ArXiv:1801.08615 [hep-ph, physics:nucl-ex, physics:nucl-th]
21. G. Scamps, et al., *Eur. Phys. J. A* **57**, 333 (2021)
22. M. Samyn, S. Goriely, P.H. Heenen, J. Pearson, F. Tondeur, *Nuclear Physics A* **700**(1-2), 142 (2002). DOI 10.1016/S0375-9474(01)01316-1
23. S. Goriely, N. Chamel, J.M. Pearson, *Phys. Rev. C* **93**, 034337 (2016)
24. W. Ryssens, et al., *Eur. Phys. J. A* **58**, 246 (2022)
25. P. Möller, A. Sierk, T. Ichikawa, H. Sagawa, *Atomic Data and Nuclear Data Tables* **109-110**, 1 (2016). DOI 10.1016/j.adt.2015.10.002. URL <https://linkinghub.elsevier.com/retrieve/pii/S0092640X1600005X>
26. M. Kortelainen, T. Lesinski, J. Moré, W. Nazarewicz, J. Sarich, N. Schunck, M.V. Stoitsov, S. Wild, *Phys. Rev. C* **82**(2), 024313 (2010). DOI 10.1103/PhysRevC.82.024313
27. H. Nakada, *Phys. Rev. C* **81**, 027301 (2010). DOI 10.1103/PhysRevC.81.027301. URL <https://link.aps.org/doi/10.1103/PhysRevC.81.027301>

Column	Quantity	Units	Explanation
1	Z	–	Proton number
2	N	–	Neutron number
3	M_{exp}	MeV	Experimental atomic mass excess
4	M_{th}	MeV	BSkG3 atomic mass excess
5	ΔM	MeV	$M_{\text{exp}} - M_{\text{th}}$
6	E_{tot}	MeV	Total energy, Eq. (1)
7	β_{20}	–	
8	β_{22}	–	Quadrupole deformation
9	β_2	–	
10	β_{30}	–	
11	β_{32}	–	Octupole deformation
12	E_{rot}	MeV	Rotational correction
13	$\langle \Delta \rangle_n$	MeV	Average neutron gap
14	$\langle \Delta \rangle_p$	MeV	Average proton gap
15	r_{BSkG3}	fm	Calculated rms charge radius
16	r_{exp}	fm	Experimental rms charge radius
17	Δr	fm	$r_{\text{exp}} - r_{\text{BSkG3}}$
18	\mathcal{I}^B	$\hbar^2 \text{MeV}^{-1}$	Calculated Belyaev MOI.
19	par(p)	–	Parity of proton qp. excitation
20	par(n)	–	Parity of neutron qp. excitation

Table 5 Contents of the Mass_Table_BSkG3.dat file.

Column	Quantity	Fission property	Units	Explanation
1	Z		–	Proton number
2	N		–	Neutron number
3	E	Inner barrier	MeV	Barrier height
4	β_{20}		–	Quadrupole deformation
5	β_{22}		–	
6	E	Outer barrier	MeV	Barrier height
7	β_{20}		–	Quadrupole deformation
8	β_{22}		–	
9	β_{30}		–	Octupole deformation
10	E	Isomer	MeV	Excitation energy
11	β_{20}		–	Quadrupole deformation

Table 6 Contents of the Fission_Table_BSkG3.dat file.

28. M. Kortelainen, J. McDonnell, W. Nazarewicz, P.G. Reinhard, J. Sarich, N. Schunck, M.V. Stoitsov, S.M. Wild, Phys. Rev. C **85**(2), 024304 (2012). DOI 10.1103/PhysRevC.85.024304
29. M. Kortelainen, J. McDonnell, W. Nazarewicz, E. Olsen, P.G. Reinhard, J. Sarich, N. Schunck, S.M. Wild, D. Davesne, J. Erler, A. Pastore, Phys. Rev. C **89**(5), 054314 (2014). DOI 10.1103/PhysRevC.89.054314
30. R. Jodon, M. Bender, K. Bennaceur, J. Meyer, Phys. Rev. C **94**(2), 024335 (2016). DOI 10.1103/PhysRevC.94.024335. URL <https://link.aps.org/doi/10.1103/PhysRevC.94.024335>
31. H. Gil, Y. Oh, C.H. Hyun, P. Papakonstantinou, New Physics: Sae Mulli **67**(4), 456 (2017). DOI 10.3938/NPSM.67.456
32. K. Bennaceur, A. Idini, J. Dobaczewski, P. Dobaczewski, M. Kortelainen, F. Raimondi, Journal of Physics G: Nuclear and Particle Physics **44**(4), 045106 (2017). DOI 10.1088/1361-6471/aa5fd7. URL <https://dx.doi.org/10.1088/1361-6471/aa5fd7>
33. P. Becker, D. Davesne, J. Meyer, J. Navarro, A. Pastore, Phys. Rev. C **96**(4), 044330 (2017). DOI 10.1103/PhysRevC.96.044330
34. P.G. Reinhard, W. Nazarewicz, Phys. Rev. C **95**, 064328 (2017). DOI 10.1103/PhysRevC.95.064328. URL <https://link.aps.org/doi/10.1103/PhysRevC.95.064328>
35. A. Bulgac, M.M. Forbes, S. Jin, R.N. Perez, N. Schunck, Phys. Rev. C **97**, 044313 (2018). DOI 10.1103/PhysRevC.97.044313. URL <https://link.aps.org/doi/10.1103/PhysRevC.97.044313>
36. K. Bennaceur, J. Dobaczewski, T. Haverinen, M. Kortelainen, Journal of Physics G: Nuclear and Particle Physics **47**(10), 105101 (2020). DOI 10.1088/1361-6471/ab9493. URL <https://dx.doi.org/10.1088/1361-6471/ab9493>
37. P. Giuliani, K. Godbey, E. Bonilla, F. Viens, J. Piekarewicz. Bayes goes fast: Uncertainty Quantification for a Covariant Energy Density Functional emulated by the Reduced Basis Method (2022). DOI 10.48550/arXiv.2209.13039
38. Q. Zhao, Z. Ren, P. Zhao, J. Meng, Phys. Rev. C **106**(3), 034315 (2022). DOI 10.1103/PhysRevC.106.034315

39. M. Baldo, L.M. Robledo, X. Viñas, *Eur. Phys. J. A* **59**, 156 (2023). URL <https://doi.org/10.1140/epja/s10050-023-01062-z>
40. L. Batail, D. Davesne, S. Péru, P. Becker, A. Pastore, J. Navarro, *Eur. Phys. J. A* **59**(7), 173 (2023). DOI 10.1140/epja/s10050-023-01073-w
41. Z.M. Niu, H.Z. Liang, *Phys. Rev. C* **106**(2), L021303 (2022). DOI 10.1103/PhysRevC.106.L021303. URL <https://link.aps.org/doi/10.1103/PhysRevC.106.L021303>. Publisher: American Physical Society
42. W. Ryssens, G. Giacalone, B. Schenke, C. Shen. Evidence of Hexadecapole Deformation in Uranium-238 at the Relativistic Heavy Ion Collider (2023). DOI 10.48550/arXiv.2302.13617
43. S. Goriely, F. Tondeur, J.M. Pearson, *Atomic Data and Nuclear Data Tables* **77**(2), 311 (2001). DOI 10.1006/adnd.2000.0857. URL <https://www.sciencedirect.com/science/article/pii/S0092646600908577>
44. P. Demorest, T. Pennucci, S. Ransom, M. Roberts, J. Hessels, *Nature* **467**, 1081 (2010)
45. T.E. Riley, et al., *ApJL* **918**, L27 (2021)
46. M.C. Miller, et al., *ApJL* **918**, L28 (2021)
47. N. Chamel, *J. Astrophys. Astron.* **38**, 43 (2017)
48. A. Sedrakian, J. Clark, *Eur. Phys. J. A* **55**, 167 (2019)
49. N. Andersson, *Universe* **7**(1) (2021)
50. L.G. Cao, U. Lombardo, C.W. Shen, N.V. Giai, *Phys. Rev. C* **73**, 014313 (2006)
51. N. Chamel, S. Goriely, J. Pearson, *Nucl Phys. A* **812**, 72 (2008)
52. N. Chamel, S. Goriely, J.M. Pearson, *Phys. Rev. C* **80**, 065804 (2009)
53. Y. Cao, S.E. Agbemava, A.V. Afanasjev, W. Nazarewicz, E. Olsen, *Phys. Rev. C* **102**(2), 024311 (2020). DOI 10.1103/PhysRevC.102.024311. URL <https://link.aps.org/doi/10.1103/PhysRevC.102.024311>. Publisher: American Physical Society
54. L.M. Robledo, G.F. Bertsch, *Phys. Rev. C* **84**(5), 054302 (2011). DOI 10.1103/PhysRevC.84.054302
55. S.E. Agbemava, A.V. Afanasjev, P. Ring, *Phys. Rev. C* **93**(4), 044304 (2016). DOI 10.1103/PhysRevC.93.044304. URL <https://link.aps.org/doi/10.1103/PhysRevC.93.044304>
56. P.A. Butler, W. Nazarewicz, *Rev. Mod. Phys.* **68**(2), 349 (1996). DOI 10.1103/RevModPhys.68.349. URL <https://link.aps.org/doi/10.1103/RevModPhys.68.349>
57. M. Bender, K. Rutz, P.G. Reinhard, J.A. Maruhn, *Eur. Phys. J. A* **8**, 59 (2000)
58. S. Goriely, M. Samyn, M. Bender, J.M. Pearson, *Phys. Rev. C* **68**, 054325 (2003)
59. D. Lunney, J.M. Pearson, C. Thibault, *Rev. Mod. Phys.* **75**, 1021 (2003)
60. M. Wang, et al., *Chinese Phys. C* **45**, 030003 (2021)
61. W. Ryssens, M. Bender, *Phys. Rev. C* **104**(4), 044308 (2021). DOI 10.1103/PhysRevC.104.044308. URL <https://link.aps.org/doi/10.1103/PhysRevC.104.044308>. Publisher: American Physical Society
62. F. Raimondi, B.G. Carlsson, J. Dobaczewski, J. Toivanen, *Phys. Rev. C* **84**(6), 064303 (2011). DOI 10.1103/PhysRevC.84.064303. ArXiv:1110.3027 [nucl-th]
63. V. Hellemans, A. Pastore, T. Duguet, K. Benhaceur, D. Davesne, J. Meyer, M. Bender, P.H. Heenen, *Phys. Rev. C* **88**(6), 064323 (2013). DOI 10.1103/PhysRevC.88.064323. URL <https://link.aps.org/doi/10.1103/PhysRevC.88.064323>
64. S. Gandolfi, G. Palkanoglou, J. Carlson, A. Gezerlis, K.E. Schmidt, *Condensed Matter* **7**(1), 19 (2022). DOI 10.3390/condmat7010019. URL <http://arxiv.org/abs/2201.01308>. ArXiv:2201.01308 [cond-mat, physics:nucl-th]
65. M. Drissi, A. Rios, *Eur. Phys. J. A* **58**(5), 90 (2022). DOI 10.1140/epja/s10050-022-00738-2. URL <https://doi.org/10.1140/epja/s10050-022-00738-2>
66. A. Schwenk, B. Friman, G.E. Brown, *Nuclear Physics A* **713**(1), 191 (2003). DOI 10.1016/S0375-9474(02)01290-3. URL <https://www.sciencedirect.com/science/article/pii/S0375947402012903>
67. E. Krotscheck, P. Papakonstantinou, J. Wang, (2023). DOI 10.48550/arXiv.2305.07096. URL <https://arxiv.org/abs/2305.07096>
68. N. Chamel, *Phys. Rev. C* **82**(1), 014313 (2010). DOI 10.1103/PhysRevC.82.014313. URL <https://link.aps.org/doi/10.1103/PhysRevC.82.014313>. Publisher: American Physical Society
69. A. Idini, G. Potel, F. Barranco, E. Vigezzi, R.A. Broglia, *Phys. Atom. Nuclei* **79**(6), 807 (2016). DOI 10.1134/S1063778816060107. URL <http://link.springer.com/10.1134/S1063778816060107>
70. F. Barranco, R.A. Broglia, G. Gori, E. Vigezzi, P.F. Bortignon, J. Terasaki, *Phys. Rev. Lett.* **83**(11), 2147 (1999). DOI 10.1103/PhysRevLett.83.2147. URL <https://link.aps.org/doi/10.1103/PhysRevLett.83.2147>
71. S.A. Fayans, D. Zawischa, *Physics Letters B* **383**(1), 19 (1996). DOI 10.1016/0370-2693(96)00716-2
72. S. Fayans, E. Trykov, D. Zawischa, *Nuclear Physics A* **568**(3), 523 (1994). DOI [https://doi.org/10.1016/0375-9474\(94\)90392-1](https://doi.org/10.1016/0375-9474(94)90392-1). URL <https://www.sciencedirect.com/science/article/pii/S0375947494903921>
73. S. Fayans, S. Tolokonnikov, E. Trykov, D. Zawischa, *Nuclear Physics A* **676**(1), 49 (2000). DOI [https://doi.org/10.1016/S0375-9474\(00\)00192-5](https://doi.org/10.1016/S0375-9474(00)00192-5). URL <https://www.sciencedirect.com/science/article/pii/S0375947400001925>
74. W. Ryssens, *Symmetry breaking in nuclear mean-field models* (PhD Thesis, Université Libre de Bruxelles, 2016)
75. W. Ryssens, M. Bender, P.H. Heenen, *Eur. Phys. J. A* **55**(6), 93 (2019). DOI 10.1140/epja/i2019-12766-6
76. D. Baye, P.H. Heenen, *J. Phys. A: Math. Gen.* **19**(11), 2041 (1986). DOI 10.1088/0305-4470/19/11/013
77. W. Ryssens, P.H. Heenen, M. Bender, *Phys. Rev. C* **92**(6), 064318 (2015). DOI 10.1103/PhysRevC.92.064318. Publisher: American Physical Society
78. J. Dobaczewski, J. Dudek, S.G. Rohozinski, T.R. Werner, *Phys. Rev. C* **62**(1), 014310 (2000). DOI 10.1103/PhysRevC.62.014310
79. I. Hamamoto, Xi zhen Zhang, Hong-xing Xie, *Physics Letters B* **257**(1-2), 1 (1991). DOI 10.1016/0370-2693(91)90847-J. URL <https://linkinghub.elsevier.com/retrieve/pii/037026939190847J>
80. C.E. Bemis, F.K. McGowan, J.L.C. Ford, W.T. Milner, P.H. Stelson, R.L. Robinson, *Phys. Rev. C* **8**(4), 1466 (1973). DOI 10.1103/PhysRevC.8.1466
81. J. Zumbro, R. Naumann, M. Hoehn, W. Reuter, E. Spera, C. Bemis, Y. Tanaka, *Physics Letters B* **167**(4), 383 (1986). DOI 10.1016/0370-2693(86)91285-2
82. N. Schunck, J. Dobaczewski, J. McDonnell, J. Moré, W. Nazarewicz, J. Sarich, M.V. Stoitsov, *Phys. Rev. C* **81**(2), 024316 (2010). DOI 10.1103/PhysRevC.81.024316
83. W. Ryssens, G. Scamps, S. Goriely, M. Bender, *Eur. Phys. J. A* **59**(5), 96 (2023). DOI 10.1140/epja/s10050-023-01002-x. URL <https://doi.org/10.1140/epja/s10050-023-01002-x>
84. S. Perez-Martin, L.M. Robledo, *Phys. Rev. C* **78**(1), 014304 (2008). DOI 10.1103/PhysRevC.78.014304

85. R. Capote, et al., RIPL - Reference Input Parameter Library for Calculation of Nuclear Reactions and Nuclear Data Evaluation **110**, 3107 (2009)
86. H. Esbensen, G.F. Bertsch, K. Hencken, Phys. Rev. C **56**(6), 3054 (1997). DOI 10.1103/PhysRevC.56.3054. URL <https://link.aps.org/doi/10.1103/PhysRevC.56.3054>. Publisher: American Physical Society
87. E. Garrido, P. Sarriguren, E. Moya de Guerra, P. Schuck, Phys. Rev. C **60**(6), 064312 (1999). DOI 10.1103/PhysRevC.60.064312. URL <https://link.aps.org/doi/10.1103/PhysRevC.60.064312>. Publisher: American Physical Society
88. P. Magierski, **2**, 57 (2019). DOI 10.2174/9781681087641119020008. URL <http://arxiv.org/abs/1606.02225>. ArXiv:1606.02225 [cond-mat, physics:nucl-th]
89. D. Peçak, N. Chamel, P. Magierski, G. Wlazłowski, Phys. Rev. C **104**(5), 055801 (2021). DOI 10.1103/PhysRevC.104.055801. Publisher: American Physical Society
90. Y. Hashimoto, G. Scamps, Phys. Rev. C **94**, 014610 (2016). DOI 10.1103/PhysRevC.94.014610. URL <https://link.aps.org/doi/10.1103/PhysRevC.94.014610>
91. A. Bulgac, P. Magierski, K.J. Roche, I. Stetcu, Phys. Rev. Lett. **116**, 122504 (2016). DOI 10.1103/PhysRevLett.116.122504. URL <https://link.aps.org/doi/10.1103/PhysRevLett.116.122504>
92. P. Magierski, K. Sekizawa, G. Wlazłowski, Phys. Rev. Lett. **119**, 042501 (2017). DOI 10.1103/PhysRevLett.119.042501. URL <https://link.aps.org/doi/10.1103/PhysRevLett.119.042501>
93. G. Wlazłowski, K. Sekizawa, P. Magierski, A. Bulgac, M.M. Forbes, Phys. Rev. Lett. **117**(23), 232701 (2016). DOI 10.1103/PhysRevLett.117.232701
94. R.C. Nayak, J.M. Pearson, Phys. Rev. C **52**(4), 2254 (1995). DOI 10.1103/PhysRevC.52.2254. Publisher: American Physical Society
95. W. Ryssens, et al., arXiv: 2211.03667, [nucl-th]. (2022)
96. S. Goriely, M. Samyn, J. Pearson, Nuclear Physics A **773**(3-4), 279 (2006). DOI 10.1016/j.nuclphysa.2006.05.002
97. M. Hukkanen, et al., arXiv: 2210.10674, [nucl-ex]. (2022)
98. S. Goriely, M. Samyn, J.M. Pearson, Phys. Rev. C **75**, 064312 (2007)
99. M. Samyn, S. Goriely, M. Bender, J.M. Pearson, Phys. Rev. C **70**(4), 044309 (2004). DOI 10.1103/PhysRevC.70.044309
100. G. Colò, N. Van Giai, J. Meyer, K. Bennaceur, P. Bonche, Phys. Rev. C **70**, 024307 (2004). DOI 10.1103/PhysRevC.70.024307. URL <https://link.aps.org/doi/10.1103/PhysRevC.70.024307>
101. L.G. Cao, U. Lombardo, P. Schuck, Phys. Rev. C **74**, 064301 (2006)
102. I. Angeli, K.P. Marinova, At. Data Nucl. Data Tables **99**, 69 (2013)
103. P. Möller, J. Nix, At. Data Nuc. Data Tables **39**, 213 (1988)
104. S. Goriely, N. Chamel, J.M. Pearson, Phys. Rev. Lett. **102**, 152503 (2009)
105. S. Goriely, N. Chamel, J.M. Pearson, Phys. Rev. C **88**(6), 061302 (2013). DOI 10.1103/PhysRevC.88.061302
106. B.N. Lu, J. Zhao, E.G. Zhao, S.G. Zhou, Phys. Rev. C **89**(1), 014323 (2014). DOI 10.1103/PhysRevC.89.014323. URL <https://link.aps.org/doi/10.1103/PhysRevC.89.014323>
107. X. Roca-Maza, X. Viñas, M. Centelles, B.K. Agrawal, G. Colò, N. Paar, J. Piekarewicz, D. Vretenar, Phys. Rev. C **92**, 064304 (2015)
108. B. Klos, et al., Phys. Rev. C **76**, 014311 (2007)
109. G. Giacalone, G. Nijs, W. van der Schee, Determination of the neutron skin of ^{208}Pb from ultrarelativistic nuclear collisions (2023). DOI 10.48550/arXiv.2305.00015. URL <http://arxiv.org/abs/2305.00015>
110. D. Adhikari, et al., Phys. Rev. Lett. **126**, 172502 (2021)
111. M. Bender, G.F. Bertsch, P.H. Heenen, Phys. Rev. C **78**, 054312 (2008)
112. M. Bender, K. Rutz, P.G. Reinhard, J.A. Maruhn, Eur. Phys. J. A **8**, 59 (2000)
113. Z.J.Z. J. Y. Zeng, T. H. Jin, Phys. Rev. C **50**, 1388 (1994)
114. A.V. Afanasjev, J. König, P. Ring, L.M. Robledo, J.L. Egido, Phys. Rev. C **62**, 054306 (2000)
115. J.M. Pearson, Y. Aboussir, A.K. Dutta, R.C. Nayak, M. Farine, F. Tondeur, Nucl. Phys. A **528**, 1 (1991)
116. National Nuclear Data Center, Nuclear structure and decay data on-line library, Nudat 2.8 (<https://www.nndc.bnl.gov/nudat2/>, 2018)
117. M. Zielinska, private communication
118. M. Rocchini, et al., Phys. Rev. C **103**, 014311 (2021)
119. M. Sugawara, et al., Eur. Phys. J. A **16**, 409 (2003)
120. A.D. Ayangeakaa, et al., Phys. Lett. B **754**, 254 (2016)
121. Y. Toh, et al., Eur. Phys. J. A **9**, 353 (2000)
122. A.D. Ayangeakaa, et al., Phys. Rev. Lett. **123**, 102501 (2019)
123. E. Clément, et al., Phys. Rev. C **75**, 054313 (2007)
124. A.E. Kavka, et al., Nucl. Phys. A **593**, 177 (1995)
125. E. Clément, et al., Phys. Rev. C **94**, 054326 (2016)
126. M. Zielińska, Ph.D. thesis, Warsaw University (2005)
127. M. Zielińska, et al., Nucl. Phys. A **712**, 3 (2002)
128. K. Wrzosek-Lipska, et al., Phys. Rev. C **86**, 064305 (2012)
129. J. Srebrny, et al., Nucl. Phys. A **766**, 25 (2006)
130. K. Wrzosek-Lipska, et al., Acta Phys. Pol. B **51**, 789 (2020)
131. C. Fahlander, et al., Nucl. Phys. A **485**, 327 (1988)
132. L.E. Svensson, et al., Nucl. Phys. A **584**, 547 (1995)
133. L. Morrison, et al., Phys. Rev. C **102**, 054304 (2020)
134. C.Y. Wu, et al., Nucl. Phys. A **607**, 178 (1996)
135. M. Chen, T. Li, J. Dobaczewski, W. Nazarewicz, Phys. Rev. C **103**(3), 034303 (2021). DOI 10.1103/PhysRevC.103.034303. URL <https://link.aps.org/doi/10.1103/PhysRevC.103.034303>. Publisher: American Physical Society
136. S.E. Agbemava, A.V. Afanasjev, Phys. Rev. C **96**(2), 024301 (2017). DOI 10.1103/PhysRevC.96.024301. URL <https://link.aps.org/doi/10.1103/PhysRevC.96.024301>. Publisher: American Physical Society
137. W. Ryssens, M. Bender, K. Bennaceur, P.H. Heenen, J. Meyer, Phys. Rev. C **99**(4), 044315 (2019). DOI 10.1103/PhysRevC.99.044315. URL <https://link.aps.org/doi/10.1103/PhysRevC.99.044315>. Publisher: American Physical Society
138. Y. Cao, S.E. Agbemava, A.V. Afanasjev, W. Nazarewicz, E. Olsen, Phys. Rev. C **102**, 024311 (2020)
139. E. Verstraelen, A. Teigelhöfer, W. Ryssens, F. Ames, A. Barzakh, M. Bender, R. Ferrer, S. Goriely, P.H. Heenen, M. Huyse, P. Kunz, J. Lassen, V. Manea, S. Raeder, P. Van Duppen, Phys. Rev. C **100**(4), 044321 (2019). DOI 10.1103/PhysRevC.100.044321. URL <https://link.aps.org/doi/10.1103/PhysRevC.100.044321>. Publisher: American Physical Society

140. C. Zhang, J. Jia, *Phys. Rev. Lett.* **128**(2), 022301 (2022). DOI 10.1103/PhysRevLett.128.022301. URL <https://link.aps.org/doi/10.1103/PhysRevLett.128.022301>. Publisher: American Physical Society
141. L.P. Gaffney, P.A. Butler, M. Scheck, A.B. Hayes, F. Wenander, M. Albers, B. Bastin, C. Bauer, A. Blazhev, S. Bönig, N. Bree, J. Cederkäll, T. Chupp, D. Cline, T.E. Cocolios, T. Davinson, H. De Witte, J. Diriken, T. Grahn, A. Herzan, M. Huyse, D.G. Jenkins, D.T. Joss, N. Kesteloot, J. Konki, M. Kowalczyk, T. Kröll, E. Kwan, R. Lutter, K. Moschner, P. Napiorkowski, J. Pakarinen, M. Pfeiffer, D. Radeck, P. Reiter, K. Reynders, S.V. Rigby, L.M. Robledo, M. Rudigier, S. Sambhi, M. Seidlitz, B. Siebeck, T. Stora, P. Thoele, P. Van Duppen, M.J. Vermeulen, M. von Schmid, D. Voulot, N. Warr, K. Wimmer, K. Wrzosek-Lipska, C.Y. Wu, M. Zielinska, *Nature* **497**(7448), 199 (2013). DOI 10.1038/nature12073. URL <http://www.nature.com/articles/nature12073>
142. B. Bucher, S. Zhu, C. Wu, R. Janssens, D. Cline, A. Hayes, M. Albers, A. Ayangeakaa, P. Butler, C. Campbell, M. Carpenter, C. Chiara, J. Clark, H. Crawford, M. Cromaz, H. David, C. Dickerson, E. Gregor, J. Harker, C. Hoffman, B. Kay, F. Kondev, A. Korichi, T. Lauritsen, A. Macchiavelli, R. Pardo, A. Richard, M. Riley, G. Savard, M. Scheck, D. Seweryniak, M. Smith, R. Vondrasek, A. Wiens, *Phys. Rev. Lett.* **116**(11), 112503 (2016). DOI 10.1103/PhysRevLett.116.112503. URL <https://link.aps.org/doi/10.1103/PhysRevLett.116.112503>
143. S. Goriely, *Eur. Phys. J. A* **51**(2), 22 (2015). DOI 10.1140/epja/i2015-15022-3. URL <http://link.springer.com/10.1140/epja/i2015-15022-3>
144. I. Kullmann, S. Goriely, O. Just, A. Bauswein, H.T. Janka. Extensive study of nuclear uncertainties and their impact on the r-process nucleosynthesis in neutron star mergers (2022). URL <http://arxiv.org/abs/2207.07421>. ArXiv:2207.07421 [astro-ph, physics:nucl-th]
145. J. Dudek, D. Curien, I. Dedes, K. Mazurek, S. Tagami, Y.R. Shimizu, T. Bhattacharjee, *Phys. Rev. C* **97**(2), 021302 (2018). DOI 10.1103/PhysRevC.97.021302. URL <https://link.aps.org/doi/10.1103/PhysRevC.97.021302>
146. N.N. Shchepochin, A.I. Chugunov, *J. Phys.: Conf. Ser.* **1697**(1), 012025 (2020). DOI 10.1088/1742-6596/1697/1/012025. URL <https://dx.doi.org/10.1088/1742-6596/1697/1/012025>. Publisher: IOP Publishing
147. N. Nikolov, N. Schunck, W. Nazarewicz, M. Bender, J. Pei, *Phys. Rev. C* **83**(3), 034305 (2011). DOI 10.1103/PhysRevC.83.034305. URL <https://link.aps.org/doi/10.1103/PhysRevC.83.034305>
148. I. Tews, J.M. Lattimer, A. Ohnishi, E.E. Kolomeitsev, *The Astrophysical Journal* **848**(2), 105 (2017)
149. H. Sagawa, S. Yoshida, L.G. Cao, *AIP Conference Proceedings* **2127**(1), 020002 (2019)
150. G. Grams, R. Somasundaram, J. Margueron, E. Khan, *Phys. Rev. C* **106**, 044305 (2022)
151. H. Gil, Y.M. Kim, P. Papakonstantinou, C.H. Hyun, *Phys. Rev. C* **103**, 034330 (2021). DOI 10.1103/PhysRevC.103.034330. URL <https://link.aps.org/doi/10.1103/PhysRevC.103.034330>
152. J. Margueron, J. Navarro, and N. Van Giai, *Phys. Rev. C* **66**, 014303 (2002)
153. N. Chamel, *Phys. Rev. C* **82**, 061307 (2010)
154. P. Danielewicz, J. Lee, *Nucl. Phys. A* **922**, 1 (2014)
155. B.T. Reed, F.J. Fattoyev, C.J. Horowitz, J. Piekarewicz, *Phys. Rev. Lett.* **126**, 172503 (2021). DOI 10.1103/PhysRevLett.126.172503. URL <https://link.aps.org/doi/10.1103/PhysRevLett.126.172503>
156. R.B. Wiringa, V. Fiks, A. Fabrocini, *Phys. Rev. C* **38**, 1010 (1988)
157. A. Akmal, V.R. Pandharipande, D.G. Ravenhall, *Phys. Rev. C* **58**, 1804 (1998)
158. Z.H. Li, H.J. Schulze, *Phys. Rev. C* **78**, 028801 (2008)
159. B. Friedman, V.R. Pandharipande, *Nucl. Phys. A* **361**, 502 (1981)
160. J.E. Lynn, et al., *Phys. Rev. Lett.* **116**, 062501 (2016)
161. S. Goriely, N. Chamel, J.M. Pearson, *Phys. Rev. C* **82**, 035804 (2010)
162. W. Zuo, A. Lejeune, U. Lombardo, J.F. Mathiot, *Nucl. Phys. A* **706**, 418 (2002)
163. T. Lesinski, K. Bennaceur, T. Duguet, J. Meyer, *Phys. Rev. C* **74**, 044315 (2006)
164. Z.H. Li, H.J. Schulze, *Phys. Rev. C* **78**, 028801 (2008)
165. X.R. Zhou, G.F. Burgio, U. Lombardo, H.J. Schulze, W. Zuo, *Phys. Rev. C* **69**, 018801 (2004)
166. T.E. Riley, et al., *ApJL* **887**, L21 (2019)
167. T.E. Riley, et al., *ApJL* **918**, L27 (2021)
168. B.P. Abbott, et al., *Phys. Rev. Lett.* **121**(16), 161101 (2018). DOI 10.1103/PhysRevLett.121.161101
169. L. Perot, N. Chamel, A. Sourie, *Phys. Rev. C* **100**(3), 035801 (2019). DOI 10.1103/PhysRevC.100.035801
170. R.C. Tolman, *Phys. Rev.* **55**, 364 (1939). DOI 10.1103/PhysRev.55.364. URL <https://link.aps.org/doi/10.1103/PhysRev.55.364>
171. J.R. Oppenheimer, G.M. Volkoff, *Phys. Rev.* **55**, 374 (1939). DOI 10.1103/PhysRev.55.374. URL <https://link.aps.org/doi/10.1103/PhysRev.55.374>
172. J.M. Pearson, N. Chamel, A.Y. Potekhin, A.F. Fantina, C. Ducoin, A.K. Dutta, S. Goriely, *MNRAS* **481**(3), 2994 (2018)
173. J.L. Zdunik, M. Fortin, P. Haensel, *Astronomy and Astrophysics* **599**, A119 (2017)
174. J. Antoniadis, et al., *Science* **340**, 6131 (2013)
175. J.M. Lattimer, C.J. Pethick, M. Prakash, P. Haensel, *Phys. Rev. Lett.* **66**, 2701 (1991)
176. G. Burgio, H.J. Schulze, I. Vidaña, J.B. Wei, *Progress in Particle and Nuclear Physics* **120**, 103879 (2021)
177. O. Komoltsev, A. Kurkela, *Phys. Rev. Lett.* **128**, 202701 (2022)
178. A. Perego, S. Bernuzzi, D. Radice, *Eur. Phys. J. A* **55**(8), 124 (2019). DOI 10.1140/epja/i2019-12810-7. URL <https://doi.org/10.1140/epja/i2019-12810-7>
179. B.N. Lu, N. Li, S. Elhatisari, D. Lee, J.E. Drut, T.A. Lähde, E. Epelbaum, U.G. Meißner, *Phys. Rev. Lett.* **125**, 192502 (2020)
180. X.L. Shang, A. Li, Z.Q. Miao, G.F. Burgio, H.J. Schulze, *Phys. Rev. C* **101**, 065801 (2020)
181. J. Keller, C. Wellenhofer, K. Hebeler, A. Schwenk, *Phys. Rev. C* **103**, 055806 (2021)
182. A. Carbone, A. Schwenk, *Phys. Rev. C* **100**, 025805 (2019)
183. S.T. Belyaev, *Nucl. Phys.* **24**, 322 (1961)
184. S. Goriely, M. Samyn, P.H. Heenen, J.M. Pearson, F. Tondeur, *Phys. Rev. C* **66**, 024326 (2002)

